Steinhöfel, G., Horn, I., von Blanckenburg, F. (2009): Micro-scale tracing of Fe and Si isotope signatures in banded iron formation using femtosecond laser ablation. - Geochimica et Cosmochimica Acta, 73, 18, 5343-5360

DOI: 10.1016/j.gca.2009.05.037

Micro-scale tracing of Fe and Si isotope signatures in banded iron formation using femtosecond laser ablation

Geochimica et Cosmochimica Act 73, 5343-5360 (2009), doi: 10.1016/j.gca.2009.05.037

Grit Steinhoefel[1]*, Ingo Horn[1], and Friedhelm von Blanckenburg[1, 2]

[1]Institut für Mineralogie, Universität Hannover, Callinstr. 3, D-30167 Hannover, Germany
[2]Present address: GFZ German Research Centre for Geosciences, Telegraphenberg, 14473 Potsdam, Germany

*Corresponding author. E-mail address: g.steinhoefel@mineralogie.uni-hannover.de

Abstract

We have detected micrometer-scale differences in Fe and Si stable isotope ratios between coexisting minerals and between layers of banded iron formation (BIF) using an UV femtosecond laser ablation system connected to a MC-ICP-MS. In the magnetite-carbonate-chert BIF from the Archean Old Wanderer Formation in the Shurugwi Greenstone Belt (Zimbabwe), magnetite shows neither intra- nor inter-layer trends giving overall uniform δ^{56}Fe values of ~0.9‰, but exhibits intra-crystal zonation. Bulk iron carbonates are also relatively uniform at near-zero values, however their individual δ^{56}Fe value is highly composition-dependent: both siderite and ankerite and mixtures between both are present, and δ^{56}Fe end member values are 0.4‰ for siderite and -0.7‰ for ankerite. The data suggest either an early diagenetic origin of magnetite and iron carbonates by the reaction of organic matter with ferric oxyhydroxides catalysed by Fe(III)-reducing bacteria; or more likely an abiotic reaction of organic carbon and Fe(III) during low-grade metamorphism. Si isotope composition of the Old Wanderer BIF also shows significant variations with δ^{30}Si values that range between -1.0 and -2.6‰ for bulk layers. These isotope compositions suggest rapid precipitation of the silicate phases from hydrothermal-rich waters. Interestingly, Fe and Si isotope compositions of bulk layers are covariant and are interpreted as largely primary signatures. Moreover, the changes of Fe and Si isotope signatures between bulk layers directly reflect the upwelling dynamics of hydrothermal-rich water which govern the rates of Fe and Si precipitation and therefore also the development of layering. During periods of low hydrothermal activity, precipitation of only small amounts of ferric oxyhydroxide was followed by complete reduction with organic carbon during diagenesis resulting in carbonate-chert layers. During periods of intensive hydrothermal activity, precipitation rates of ferric oxyhydroxide were high, and subsequent diagenesis triggered only partial reduction, forming magnetite-carbonate-chert layers. We are confident that our micro-analytical technique is able to detect both the solute flux history into the sedimentary BIF precursor, and the BIF's diagenetic history from the comparison between coexisting minerals and their predicted fractionation factors.

1. Introduction

Banded iron formations (BIFs) are chemical marine sediments that formed periodically throughout the Precambrian (3.8 to 0.5 Ga) and are usually characterized by alternating Fe- and Si-rich layers. The peak in BIF formation between 2.5 and 2.3 Ga appears to correlate with major changes in the Earth's history such as the rise of atmospheric oxygen and the change from anoxic to oxic conditions in the ocean (Canfield, 2005; Holland, 2006). BIFs are the product of chemical precipitation from seawater and subsequent depositional, diagenetic and metamorphic processes. Because of this extraordinary record of the early Earth, it is of major interest to understand the genetic history of BIFs.

The investigation of light stable isotope systems in BIFs, namely O, C and S isotope ratios, has a long tradition (e.g. Becker and Clayton, 1972, 1976; Perry et al., 1973, 1978; Goodwin et al., 1976; Baur et al., 1985; Beukes et al., 1990; Kaufman et al., 1990; Mojzsis et al., 1996; Fedo et al., 2006). In recent years, advances in analytical techniques have provided the opportunity to study the stable isotope fractionation of the two major elements in BIFs, Fe and Si. The investigation of fractionation mechanisms of stable Fe isotopes is now well-advanced, and shows an overall range of ~5 ‰ in δ^{56}Fe (for overview see Anbar, 2004; Beard and Johnson, 2004; Dauphas and Rouxel, 2006). The largest variability in the Fe isotope composition in any single type of sample has so far been measured in BIFs (Johnson et al., 2003, 2008; Dauphas et al., 2004, 2007; Rouxel et al., 2005; Frost et al., 2007; Whitehouse and Fedo, 2007; Valaas Hyslop et al., 2008) and ranges from about -2.5 to 1.6‰ in δ^{56}Fe. It has been shown that Fe isotope heterogeneities in BIFs can be preserved during diagenesis and metamorphism (Frost et al., 2007; Whitehouse and Fedo, 2007). Magnetite, for example, appears to be of diagenetic origin and

preserves its Fe isotope signature throughout all but the highest grades of prograde contact metamorphism (Frost et al., 2007). Therefore, Fe isotopes appear to be a powerful tool for the reconstruction of the early history of BIF deposition, and much effort is now being directed at deciphering the underlying processes that have caused their heterogeneous Fe isotope composition. For example, the appearance of BIFs that are depleted in heavy Fe isotopes have been interpreted as evidence for bacteria-mediated Fe reduction during diagenesis (Johnson and Beard, 2006; Johnson et al., 2008). Dissimilatory Fe reduction appears to be a significant form of metabolism since at least 2.9 Ga (Vargas et al., 1998). In contrast, BIFs which are enriched in heavy Fe are regarded to reflect partial oxidation of Fe in the upper levels of ocean water (Dauphas et al., 2004; 2007; Johnson and Beard, 2006; Johnson et al., 2008).

The variability of stable Si isotope ratios has also been explored in natural systems, with an overall fractionation of ~12‰ in δ^{30}Si (for overview see André et al., 2006; van den Boorn et al., 2007). However, experiments on processes and degrees of Si isotope fractionation are yet to be carried out. Chert within BIFs exhibits a largely negative Si isotope signature ranging from about -2.5 to -0.5‰ in δ^{30}Si which has been interpreted as a hydrothermal signal (Jiang et al., 1993; Ding et al., 1996; André et al., 2006). Positive δ^{30}Si values in Precambrian chert may reflect elevated temperature of the seawater, the influence of a continental source, or precipitation from isotopically heavy seawater (Robert and Chaussidon, 2006; van den Boorn et al., 2007).

The questions posed by these studies generally revolve around the relative impact of variable source isotope compositions as opposed to those caused by diagenesis. In previous studies, these issues are left unresolved, to some extent, by the experimental approach which is mostly based on bulk rock or bulk mineral concentrate analysis and may obscure small-scale fractionation processes within layers of a BIF or temporal developments between layers. These issues may be resolved by an increased spatial resolution of the measurement. In this study, we present the results on the first in situ determination of Fe and Si isotope compositions using an UV femtosecond laser ablation system coupled to a multicollector inductively coupled plasma mass spectrometer (MC-ICP-MS). The advantage of this in situ method is the high spatial resolution while maintaining a high precision of the isotope ratio measurement. This approach provides the opportunity to investigate potential small-scale temporal trends and processes as based on the composition of individual mineral phases. We show that small-scale intra-layer fractionations are of diagenetic origin, while secular trends in the BIF stratigraphy reveal the source of the contributing fluids.

2. Investigated BIF

The investigated sample material represents an Algoma-type iron formation from the Wanderer Formation within the late Archean Shurugwi Greenstone Belt in Zimbabwe and was collected from the Old Wanderer Mine (Fig. 1). The Shurugwi Greenstone Belt belongs to the Bulawayan Supergroup, a well-preserved greenstone belt sequence in the Zimbabwe craton. Isotope age data of this sequence range from 2.88 to 2.65 Ga (Moorbath et al., 1987; Wilson et al., 1995). The evolution and the tectonic setting of the Bulawayan Greenstone Belt Sequence are still subjects to controversy. It is now generally believed that the belt is associated with a passive continental margin setting and the interaction of mantle plumes during the beginning continental break-up (Prendergast, 2004).

The Wanderer Formation is a sequence of clastic and chemical sediments with a number of ore bodies of approximately 100 m in thickness, which partly contain gold mineralizations (Tyndale-Biscoe, 1949; Foster and Gilligan, 1987). The iron formation within this succession is described as a mixed silicate-carbonate facies. The chondrite-normalized rare earth element (REE) distribution of this iron formation exhibits a flat pattern with a distinct positive Eu-anomaly and depleted absolute concentrations which is typical for Archean Fe-rich sediments (Oberthuer et al., 1990). The presence of positive Eu-anomalies in BIFs indicates a dominant high-temperature hydrothermal source for Fe (Bau and Dulski, 1996). Gold mineralizations occur mainly in phyllite. They are rare in iron formation, where they are associated with high abundance of secondary iron sulphide (Tyndale-Biscoe, 1949; Oberthuer et al., 1990). The metamorphic overprint of this area is at the most greenschist facies as conversion of chlorite to biotite is rare in phyllite (Tyndale-Biscoe, 1949).

The magnetite-carbonate-chert BIF investigated in this study (Fig. 2) is pristine: primary textures and structures are well preserved, replacements of secondary iron sulfides are absent, and quartz occurs in the form of microcrystalline chert. Layers of several millimetres thickness are composed of variable amounts of chert, iron carbonates (siderite and ankerite), magnetite, and minor pyrite and chlorite (Fig. 3, Table 1). Greenish layers are magnetite-rich with minor chlorite. Fe concentrations are high with ~35 wt.%. In these layers, the chemical composition of iron carbonates is dominated by siderite; ankerite is a minor constituent. Light layers are dominated by iron carbonate and chert and contain no magnetite. These layers exhibit much lower Fe concentrations of ~10 wt.%, and ankerite and siderite may reach equal proportions. The chemical compositions of magnetite, siderite and ankerite have been investigated by electron microprobe and are presented in Table 2. The very pure magnetite of stoichiometric composition exhibits grains of 10 to 50 µm in diameter with sub- to euhedral habit and is concentrated within well-defined bedding planes. Iron carbonate occurs as siderite, $(Fe_{0.75-0.90}, Mg_{0.10-0.25})CO_3$, and ankerite, $Ca(Fe_{0.60-0.75}, Mg_{0.25-0.40})(CO_3)_2$, in variable proportions. Both types of iron

carbonates exhibit chemically zoned crystals indicating a complex growth history. In the thin section, cores of irregular shape show distinct transitions to interlocked overgrowths which differ in the relative proportion of Mg and Fe (Fig. 2b). Average chemical compositions of the two siderite and ankerite varieties, respectively, are given in Table 2. Xenomorphic quartz occurs in form of microcrystalline chert grains with grain-sizes between 5 to 50 µm in diameter. Assuming similar depositional rates as estimated for other BIF deposits (Trendall et al., 2004, Pickard 2002; 3003), the investigated thin section may represent some 10^2 to 10^3 years of deposition.

3. Methods

The Fe and Si isotope compositions of major Fe-bearing minerals and chert, respectively, were determined by in situ femtosecond laser ablation ICP-MS (LA-ICP-MS) measurements at a high spatial resolution. Fe isotope ratios of bulk mineral separates were also measured by solution ICP-MS. All isotope ratios were determined on a Thermo Finnigan Neptune MC-ICP-MS at the Leibniz University of Hannover and corrected for the instrumental mass discrimination using standard-sample-bracketing. The data are reported as δ^{56}Fe and δ^{30}Si relative to the reference materials IRMM-014 and NBS28, respectively.

$$\frac{\delta^{56}Fe}{‰} = \left(\frac{{}^{56}Fe/{}^{54}Fe_{Sample}}{{}^{56}Fe/{}^{54}Fe_{IRMM-014}} - 1 \right) * 1000 \quad (1)$$

$$\frac{\delta^{30}Si}{‰} = \left(\frac{{}^{30}Si/{}^{28}Si_{Sample}}{{}^{30}Si/{}^{28}Si_{NBS28}} - 1 \right) * 1000 \quad (2)$$

3.1. *In situ* LA-ICP-MS

The Fe and Si isotope composition of the different mineral phases of the investigated BIF were determined using our in-house built UV femtosecond laser ablation system coupled to a Thermo Finnigan Neptune MC-ICP-MS. The laser ablation system is based on an amplified frequency-quadrupled femtosecond laser (Spectra Physics Hurricane I, USA) operating at a wavelength of 196 nm which avoids laser-induced isotope and elemental fractionation and minimizes the matrix dependency of analyses (Horn and von Blanckenburg, 2007). The accuracy and precision for Fe and Si isotope measurements have been verified for different types of matrices by Horn et al. (2006) and Chmeleff et al. (2008), respectively. Fe isotope ratios were determined by spot analysis with a diameter of 18 to 35 µm. For an average signal of 10 V for ^{56}Fe on a faraday cup equipped with a 10^{11} Ω resistor, a spot analysis of 2 minutes creates a crater of ~8 µm depth at a diameter of 30 µm in pure iron (reference material IRMM-014). A total consumption of ~45 ng Fe per analysis can be calculated. Because ion beam intensities between standard and sample materials should be matched, the analysis of minerals with lower Fe concentrations demands higher repetition rates resulting in a greater crater depth. The Si isotope ratios were measured in the raster mode using a spot size of ~35 µm. The raster size was about 50 µm x 500 µm. The ablated volume is ~36x10^3 µm^3 for quartz giving a consumption of ~50 ng Si per analysis (Chmeleff et al., 2008). The acquisition parameters were set to acquire 30 to 60 cycles per analysis, with a cycle integration time of 2 seconds using the medium mass resolution for the mass spectrometer. The potential tapping of different phases during ablation are identified from shifts in the isotope ratios and/or variations in signal intensity, and such measurements were discarded.

3.1.1. Fe isotope measurements

The Fe isotope composition of magnetite, siderite and ankerite were determined following the analytical procedure of Horn et al. (2006). Previous investigations have shown that the overall reproducibility of different types of matrixes including iron oxides and iron carbonates is better than ± 0.1‰ (2 SD) for δ^{56}Fe and that the results are consistent with those obtained by conventional solution ICP-MS measurements (Horn et al., 2006). Over the course of 9 months, replicated spot analyses of the metal standard Puratronic (Johnson Matthey) resulted in mean values of 0.08‰ for δ^{56}Fe and 0.12‰ for δ^{57}Fe relative to IRMM-014, with an external precision of ± 0.08 and ± 0.14‰, respectively (2 SD, n=101) (Fig. 4). This agrees well with the average value of 0.09 ± 0.05 ‰ for δ^{56}Fe (2 SD, n=4) and 0.13 ± 0.08‰ for δ^{57}Fe (2 SD, n=4) obtained by solution ICP-MS measurements in our laboratory. The data show a Gaussian distribution and plot along the theoretical fractionation line for δ^{56}Fe versus δ^{57}Fe which confirms the long-term accuracy and reproducibility of the LA-ICP-MS measurements.

The Fe isotope measurements by LA-ICP-MS on the BIF sample were carried out as follows. Magnetite crystals were analysed by spot analyses (Fig. 2b, 3). The size of the crater ranged between 25 and 35 µm in diameter. The analyses were performed preferentially along the boundaries between layers to disclose potential intra-layer isotope trends but a number of analyses were also carried out in the center of the layers. Siderite and ankerite were analysed using the raster mode or short line scans on areas of 50 µm x 50 µm to 100 µm x 100 µm (Fig. 3). To detect potential isotope zonation within single magnetite crystals (< 50 µm), we developed a new analytical procedure that involves sequential coring - the core of the mineral phase is determined first using a spot diameter of 18 to 25 µm. In a second step, a spot analysis with a diameter of ~35 µm is superimposed onto the same location. This step removes a ring of material around the pit of the first analysis and determines the Fe isotope composition of the outer part (rim) of the mineral phase for a cubic crystal structure. This procedure was validated prior to the analysis of magnetite using the spatially homogeneous metal standard Puratronic (Johnson Matthey). Figure 5 shows the result of 13 pairs of such core-rim analyses on the metal standard Puratronic in terms of their $\delta^{56}Fe$ compositions. The mean of $\delta^{56}Fe_{core}$ and $\delta^{56}Fe_{rim}$ is determined at 0.07 ± 0.08‰ and 0.06 ± 0.17‰, respectively, showing no significant difference of the distributions (two-sample Student‘s t-test, 95% confidence level). This result indicates that femtosecond laser-induced lateral damages or alterations of the material surrounding an ablation crater are undetectable at a precision level of 0.1‰ (2 SD) with respect to the Fe isotope composition.

3.1.2. Si Isotope measurements

The Si isotope composition were investigated in chert by LA-ICP-MS using the method described in detail by Chmeleff et al. (2008) which is similar to that of Fe isotope analysis. Accuracy and precision have been previously verified for different types of matrices including quartz giving a overall reproducibility of 0.24‰ (2 SD) for $\delta^{30}Si$ (Chmeleff et al., 2008). Chert was analysed by narrow rasters of about 50 µm x 500 µm to reach a high spatial resolution perpendicular to the layering (Fig. 3).

3.2. Solution ICP-MS

In addition to LA-ICP-MS, the Fe isotope composition of iron carbonate and magnetite was investigated as bulk mineral leachates for several layers by solution ICP-MS. Individual layers were sampled using either a diamond tipped core bit or tungsten carbide mirco-drill bits. The extracted material was crushed in an agate mortar if necessary and the different mineral phases were separated and dissolved as follows. The magnetite was removed magnetically and dissolved in aqua regia. Carbonates were leached with 10% acetic acid at 35°C to avoid dissolution of minor iron phases as chlorite, pyrite and any residual magnetite following the procedure of von Blanckenburg et al. (2008). Dissolution tests conducted under the same conditions have shown that 10% acetic acid does not dissolve magnetite, other iron oxides or pyrite. Layer 6 was used to test whether siderite and ankerite, exhibiting widely different isotope composition when analysed in situ (Table 3, Fig. 6a, b), are leached in representative proportions. The calculated Fe isotope composition for bulk iron carbonate (based on estimated modal abundances of siderite and ankerite, their average Fe contents and their isotope compositions obtained by LA-ICP-MS) is -0.02‰ – this value shows no significant difference to 0.09‰ determined by solution ICP-MC and the leachates are considered representative. The Fe isotope composition of magnetite and iron carbonate were determined after chemical purification following the procedure described by Schoenberg and von Blanckenburg (2005). The obtained long-term external reproducibility of the solution ICP-MS measurements is better than ± 0.05‰ (2 SD).

4. Results

4.1. Fe isotope composition

The Fe isotope compositions of the major Fe-bearing mineral phases are presented in Table 3 and Figures 6a, b and 7. Solution ICP-MS of magnetite exhibits $\delta^{56}Fe$ values of 0.82‰ to 1.00‰. LA-ICP-MS reveals significant variation in the magnetite Fe isotope composition in lateral as well as in vertical directions. However, Fe isotope compositions averaged over entire layers are surprisingly uniform (Fig. 6b). Comparison of the standard deviation of magnetite populations with the standard deviation of a dataset obtained from homogeneous material shows that in most cases the variations exceed the analytical precision. This demonstrates that small-scale variations in magnetite-rich layers exist, and can be measured. The maximal observed range within a stratigraphic level is 0.45‰ to 0.76‰ in $\delta^{56}Fe$ giving a mean of 0.66 ± 0.18‰ (2 SD, n=11). Standard deviations of magnetite populations range from ± 0.08 to 0.21‰ (2 SD, n=5 to 17). The means of the layers obtained by LA-ICP-MS range from 0.71 to 1.02‰. Although heterogeneities exist, neither intra- nor inter-layer trends can be observed within layers 9 to 15, in which more than 5 analyses have been performed. Taking all spot analyses obtained in these layers, the dataset shows a Gaussian distribution giving an average of 0.72 ± 0.17‰ (2 SD,

n=77) (Fig. 7).
The magnetite crystals are internally heterogeneous in their Fe isotope composition, as revealed in layer 13 by the sequential coring method (Fig. 5). Depending on the cut of the magnetite crystals in the thin section, the cores are up to 0.3‰ lighter in their Fe isotope composition than the rims. The mean $\delta^{56}Fe_{core}$ is 0.75 ± 0.13‰ (2 SD, n=21) which presents a resolvable difference from the mean $\delta^{56}Fe_{rim}$ of 0.89 ± 0.24‰ (2 SD, n=18) (two-sample Student's *t*-test, 95% confidence level).
Comparing average LA and solution ICP-MS measurements of magnetite in designated layers (Table 3, Fig. 6b), the solution data appear to indicate a slightly heavier Fe isotope composition than the corresponding LA data. This discrepancy can be explained by the isotope zonation found in magnetite crystals. Spot analyses are usually placed away from crystal edges to avoid mixing of different phases. Because the outer rim is also the isotopically heaviest part of the crystals, the LA data is biased towards lighter compositions.
The iron carbonates were investigated in several layers via bulk mineral solution ICP-MS. The δ^{56}Fe values range from -0.13 to 0.25‰ giving an average of about 0‰. LA-ICP-MS of siderite and ankerite show significant variations in their Fe isotope composition. Because pure iron carbonate phases are usually smaller than the area required for a LA analysis and cannot easily be distinguished from each other using the optical microscope integrated in the LA system, most analyses are likely to represent mixtures of siderite and ankerite. As expected from their distinct chemical composition with variable degrees of Mg- and Ca-substitution, Fe isotope compositions vary. Ankerite shows values which are always isotopically lighter when compared to siderite within a given layer. If we assume the lowest δ^{56}Fe values to represent the best estimate of ankerite compositions, whereas the highest δ^{56}Fe corresponds to those of the siderite end member, then ankerite exhibits δ^{56}Fe values as low as -0.70‰, whereas siderite shows consistently positive δ^{56}Fe values of up to 0.43‰. The relative difference of δ^{56}Fe observed in layers where both mineral phases were examined is ~0.4‰ to 1.1‰.
The difference in δ^{56}Fe between magnetite and bulk iron carbonate in magnetite-rich layers where the dominant carbonate phase is siderite appears to be relatively uniform with ~0.9‰. The Fe isotope composition of bulk layers can be calculated from Fe isotope data of the major Fe-bearing mineral phases, their estimated modal abundances, and Fe contents (grey bars in Fig. 6b, Table 1). Magnetite-rich layers have average δ^{56}Fe values between 0.22‰ and 0.76‰, whereas carbonate layers are generally lighter in their Fe isotope composition with δ^{56}Fe values of -0.04‰ to 0.25‰.

4.2. Si isotope composition

The Si isotope data are presented in Table 4 and Figure 6c. Chert in the investigated BIF exhibits strong variations in its Si isotope composition perpendicular to layering giving a mean δ^{30}Si value of -1.56 ± 0.76‰ (2 SD, n = 57). The calculated mean composition of the layers ranges between -1.04‰ to -2.55‰. Intra-layer variations are minor with ± 0.09‰ to ±0.44‰ (2 SD), which is close to the achievable precision of ± 0.24‰ (2 SD).

5. Discussion

5.1. Significance of bulk Fe and Si isotope composition in the Old Wanderer BIF

The overall Fe and Si isotope compositions of the 2.7 Ga Old Wanderer BIF is within the observed range of previously investigated BIFs (see overviews in André et al., 2006; Johnson and Beard, 2006; van den Boorn et al., 2007). Iron carbonates with a bulk Fe isotope composition of ~0‰ and magnetite with δ^{56}Fe of ~0.9‰ reveal an overall enrichment in heavy Fe isotopes. Chert displays an overall depleted Si isotope signature, even though strong inter-layer variations exist ranging from -1.04 to -2.55‰ in δ^{30}Si.
Although the geochemical cycles of Fe and Si in the Precambrian are still poorly understood it is clear that they differed from that of the Phanerozoic. Under anoxic conditions in Precambrian ocean, the Fe concentration in seawater would have been much higher than today, between 2 and 50 ppm (Ewers, 1983; Sumner, 1997; Canfield, 2005). The abundance of iron oxides requires oxidation in a largely anoxic ocean which is generally explained by a stratified ocean system with an oxidising upper water column (e.g. Klein, 2005). Oxidation and subsequent precipitation of ferric oyxhydroxide was most likely caused by anaerobic photosynthesis (e.g. Konhauser et al., 2002; Kappler et al., 2005) or atmospheric oxygen (e.g. Holland, 1973; Drever, 1974; Ehrenreich and Widdel, 1994; Kaufman et al., 2007). In the absence of silica-secreting organisms, the Si concentration in the Precambrian ocean could have been as high as 110 ppm, the saturation state of amorphous silica (Maliva et al., 2005). Therefore the direct precipitation of silica from seawater in form of siliceous gel is the most likely Si removal process. Sorption of silica on clay minerals, iron oxides, or organic matter may have played a role in the nucleation and/or precipitation (Perry and Lefticariu, 2003; Konhauser et al., 2007).
BIFs within greenstone belts, such as the Old Wanderer BIF, are generally regarded to have formed in close vicinity to hydrothermal systems (e.g. Klein, 2005). In this regard, we can assume a predominantly hydrothermal fluid source providing the solutes, from which the sedimentary BIF precursor was precipitated. This is certainly

suggested by REE patterns showing a positive Eu-anomaly which is interpreted as hydrothermal signature (Bau and Dulski, 1996; Oberthuer et al., 1990). Si isotopes are also compatible with a hydrothermal origin. Despite vent fluids carry Si with δ^{30}Si of -0.2 to -0.4‰ (De La Rocha et al., 2000), silica-rich deposits precipitated around oceanic smokers are even lighter with δ^{30}Si of -1.6 ± 0.7‰ (2 SD, n=25) (Ding et al., 1996). This compares well to the mean δ^{30}Si measured in the Old Wanderer BIF which is strongly negative at -1.56 ± 0.76‰ (2 SD, n=57). Fe isotopes can also be explained by precipitation from a hydrothermal Fe source. δ^{56}Fe values measured in hydrothermal fluids typically range between -0.6 and -0.2‰ (Sharma et al., 2001; Beard et al., 2003; Severmann et al., 2004) with higher values corresponding to high Fe concentrations. Together with a presumably higher Precambrian hydrothermal flux, an elevated heat flux (Bau and Möller, 1993) and minimal oxidation rate close to the vent site under anoxic conditions, Johnson et al. (2008) have argued that ancient hydrothermal fluids would have exhibited a Fe isotope composition closer towards bulk oceanic crust, i.e. near-zero. This is roughly the composition of bulk Fe in the Old Wanderer BIF.

However, given that both Fe and Si precipitated simultaneously but with variable intensity as BIFs are characterized by alternating Fe-rich and Si-rich layers, their isotope fractionations must be considered together. The precipitation of amorphous silica favours light Si (De La Rocha et al., 1997; Ziegler et al., 2005; Basile-Doelsch, 2006). Fe precipitation by partial oxidation is dominated by ferric oxyhydroxide which is ~1.5‰ heavier than $Fe(II)_{aq}$ (Bullen et al., 2001; Skulan et al., 2002; Welch et al., 2003; Croal et al., 2004; Anbar et al., 2005). Potential Fe and Si isotope fractionation of the precipitates is illustrated in Figure 8. Considering the presumably long residence times for both Fe and Si in the order of 10^6 years (Siever, 1992; Trendall, 2002), steady state conditions of the ocean are likely and short-term changes of well-mixed seawater within the deposition time of some 10^2 to 10^3 years for the investigated BIF section are unexpected. In this case, a steady state system must exist between hydrothermal influx and chemical deposition.

In the Old Wanderer BIF, however, steady state conditions have not been attained as bulk layers, which reflect presumably primary signatures (see *section 5.2.*), are variable in their isotope compositions and differ in most cases from the hydrothermal signature. It is more likely that the residence time of both Fe and Si was short relative compared to precipitation time scales, and that pulses of hydrothermal emanations triggered episodic recharge and precipitation events. The result is that the degree of Fe and Si depletion of hydrothermal solutions can be variable, and Rayleigh distillation style modifications become visible in the Fe and Si isotope signatures. Therefore, both seawater and sediment composition depend on the fraction of Fe and Si precipitation. Because steady state is never achieved, isotope ratios of the precipitates are between those of the hydrothermal fluid (for complete precipitation) and the fractionation factor $\Delta_{precipitate\text{-}solution}$ (for incomplete precipitation). The data of the Old Wanderer BIF indicate high fractions of Fe precipitation (ca. 85-100%) whereas those of Si are low (ca. 1-40%) (Fig. 8). This is compatible with a situation in which Si is precipitated by saturation from the entire water column of an episodically discharged hydrothermal plume, whereas Fe is almost entirely precipitated as ferric oxyhydroxide, the precursor of magnetite and iron carbonate (see *section 5.2.*), via $Fe(II)_{aq}$ oxidation of the plume in the upper water column.

Surprisingly perhaps, δ^{56}Fe and δ^{30}Si values of bulk layers are covariant with a correlation factor of 0.71, significant at the confidence level of 95% (Figs. 6 and 8, Table 1). However, given the opposite precipitation fractionation factors for Fe oxidation and Si precipitation, one may expect an anticorrelation.

The only plausible explanation for this phenomenon is one in which high fractions of Fe precipitation are simultaneous in space and time with low fractions of Si precipitation, and vice versa. An example is shown by the model curve in Figure 8, in which the fraction of precipitated Fe is always opposite to that of precipitated Si.

Figure 9 shows a possible scenario of an episodically active hydrothermal system. At periods of low plume dispersion (Fig. 9a), silica precipitation occurs from a largely unaffected fluid near the venting site causing strongly negative δ^{30}Si values, whereas the low supply of Fe to the oxidizing upper water column promotes complete oxidation resulting in ferric oxyhydroxide with δ^{56}Fe values close to the hydrothermal signature, i.e. near-zero. This situation is compatible with the origin of carbonate-chert layers which exhibit low Fe contents together with low δ^{56}Fe and δ^{30}Si values relative to magnetite-rich layers. An extreme situation might be reflected by pure chert layers of exceptionally low δ^{30}Si values, i.e. layer 4 reveals –2.55‰. In this case, the hydrothermal plume dispersion might be limited to the lower water column preventing Fe precipitation.

In periods, the upwelling plume reaches the surface of the ocean (Fig. 9b), the fluid is modified by ongoing silica precipitation causing Rayleigh distillation or by mixing with ambient seawater with a strong positive isotope composition. Both shift the isotope signature of the precipitating silica towards heavier values (André et al., 2006; van den Boorn et al., 2007). The supply of large quantities of $Fe(II)_{aq}$ into the upper water column triggers partial oxidation as the oxidant becomes the limiting factor resulting in high rates of ferric oxyhydroxide formation with positive δ^{56}Fe values. Such a situation might be reflected in magnetite-carbonate-chert layers. They show significantly higher Fe contents together with significantly positive δ^{56}Fe and increased δ^{30}Si values compared to carbonate-chert-layers. This model of an episodically recharged hydrothermal plume explains the Fe and Si signatures of the Old Wanderer BIF but of course fractionation factors and source compositions that change with time cannot be excluded.

5.2. Diagenesis and the formation of magnetite and iron carbonate

The origin of magnetite and iron carbonates in BIFs is controversial and may involve more than one formation pathway as revealed from Fe isotope signatures (Johnson et al., 2008). Magnetite possibly originates from a primary hydro-magnetite precursor (Klein, 2005) but more likely through biomineralization or diagenetic processes. Nano-particles of magnetite can be precipitated either intra-cellularly by magnetotactic bacteria (e.g. Karlin et al., 1987; Chang et al., 1989; Konhauser, 1998) or, more efficiently, by extracellular processes due to dissimilartory Fe reduction (DIR) of Fe(III) by oxidation of organic matter (e.g. Lovley, 1997; Konhauser et al., 2005). Further pathways involve the abiotic reduction of Fe(III) (e.g. Perry et al., 1973; Morris, 1993). Alternatively, magnetite incorporates hydrothermal Fe(II) (Ohmoto, 2003). Siderite is regarded either as direct precipitate from seawater (Klein and Beukes, 1989; Kaufman et al., 1990; Klein, 2005; Sumner, 1997) or diagenetic product possibly coupled to the formation of magnetite (Ewers and Morris, 1981; Lovley, 1990, 1991).

The advantage of Fe isotope analyses of coexisting mineral phases is that they allow one to infer these processes. For example, independent formation pathways of magnetite and siderite result in Fe isotope disequilibrium, whereas coupled diagenetic formation of magnetite and siderite by biotic or abiotic reduction of Fe(III) have to show Fe isotope equilibrium in coexisting mineral phases. The comparison of measured Fe isotope differences of coexisting mineral phases with published fractionation factors (see Table 5) enables us to identify formation processes.

The direct formation of iron carbonates from seawater appears unlikely in the light of the isotope fractionation factors for Fe(II) incorporation into carbonate. Although the equilibrium fractionation factor is still not well constrained, siderite seems to prefer light Fe(II) relative to $Fe(II)_{aq}$; an ankeritic component increases the fractionation factor (see Table 5 for references). $\delta^{56}Fe$ values of bulk iron carbonates (siderite + ankerite) in the Old Wanderer BIF cluster around 0‰ which requires ancient seawater with a heavier $\delta^{56}Fe$ value than measured for iron carbonates. Taking the equilibrium fractionation factor of Wiesli et al. (2004), the ancient seawater would have had a heavy $\delta^{56}Fe$ value of at least 0.4‰ to 0.6‰ which is inconsistent with a strong hydrothermal influence suggesting a Fe isotope signature of the seawater of not more than 0‰.

The most likely scenario is a largely simultaneous diagenetic or metamorphic formation of magnetite and siderite. Both would have formed from a common precursor substrate by the partial reduction of previously precipitated ferric oxyhydroxides by oxidation of organic matter (Han, 1978; Perry et al., 1973; Ewers and Morris, 1981; Lovley, 1991). Given that coexisting magnetite and siderite in the investigated sample show a uniform relative difference of ~0.9‰ and that this difference agrees with that expected from isotope equilibrium fractionation (see Table 5), the coupled formation under equilibrium conditions is suggested. The Fe(II) released by reduction reacts either with residual ferric (hydr)oxides to produce magnetite or with bicarbonate to form siderite. Several studies of C isotope compositions in Precambrian BIFs indicate that extensive magnetite and iron carbonate deposition resulted from organic carbon oxidation coupled to Fe(III) reduction (Perry et al., 1973; Walker, 1984; Baur et al., 1985; Kaufman et al., 1990). In this process, layering is of diagenetic origin that is controlled by the relative amount of organic matter to ferric (hydr)oxide in a given layer. This ratio controls the degree of ferric (hydr)oxide dissolution and the pH-Eh conditions and therefore the abundance of siderite and magnetite (Fig. 9).

An early diagenetic pathway involves dissimilatory Fe reducing bacteria which use Fe(III) as electron donor when oxidizing organic matter to produce energy (Lovley et al., 1987; Lovley, 1990, 1991; Roden, 2004; Konhauser et al., 2005). In the Old Wanderer BIF, magnetite - siderite pairs show a relative difference of ~0.9‰. Very similar values have been reported for the Kuruman BIF in the Transvaal Basin, South Africa (Johnson et al., 2003), and the Biwabik BIF (Frost et al., 2007) which have been interpreted as resulting from a coupled diagenetic formation process of siderite and magnetite due to DIR. Experimental work by Johnson et al. (2005) has revealed an equilibrium fractionation factor $\Delta_{siderite\text{-}magnetite}$ of -1.3‰ for DIR, whereas Johnson et al. (2008) prefer a fractionation factor of -1.8‰ (see Table 5). An ankeritic component would increase the fractionation factor (Polyakov and Mineev, 2000; Johnson et al., 2005, see Table 5). Both fractionation factors are considerable higher than the observed difference which may either indicate that another process is involved or the formation of magnetite and iron carbonates occurred at an elevated temperature.

Alternatively, magnetite and siderite might have formed by abiotic reduction of ferric (hydr)oxides by oxidation of organic matter during late diagenesis or low-grade metamorphism (Perry et al., 1973; Morris, 1993; Frost et al., 2007). Predictions from Mössbauer data (Polyakov and Mineev, 2000; Mineev et al., 2007; Polyakov et al., 2007) give an equilibrium fractionation factor $\Delta_{siderite\text{-}magnetite}$ between -1.8 and -2.8‰ at 22°C which decreases to -0.8 to -1.2‰ at 200°C (Table 5). This elevated-temperature estimate is consistent with the observed difference of -0.9‰ in magnetite-rich layers.

Ankerite is considered as late diagenetic phase forming at the expense of siderite (e.g. Kaufman et al., 1990). Both experimental and Mössbauer approaches indicate that ankerite incorporates lighter Fe(II) than siderite under equilibrium conditions (see Table 5). This is also observed in the Old Wanderer BIF, where ankerite is

0.4‰ to 1.1‰ lighter in its isotope composition than siderite.
Major post-depositional redistribution of Si and Fe, such as recycling to the ocean or equilibration across layering in the course of diagenetic/metamorphic processes, appears unlikely in the Old Wanderer BIF. The significant variations in δ^{30}Si for chert on a millimeter-scale supports the notion that Si isotopes are largely unaffected, and that chert preserves the primary isotope signature (André et al., 2006; van den Boorn et al., 2007).
Redistribution of Fe across layering can potentially be caused by different degrees of ferric (hydr)oxide reduction which produces gradients in $Fe(II)_{aq}$ activity and pH conditions and drive diffusion of $Fe(II)_{aq}$ perpendicular to layers (Ewers, 1983). However, evidence from this sample as well as evidence from other BIFs (Frost et al., 2007; Johnson et al., 2008) suggest that mineral phases from adjacent layers in BIFs did not form in Fe isotope equilibrium and that significant isotope exchange in BIF across layering is absent. In the 1.9 Ga old Biwabik Iron Formation, differences in the oxygen fugacity and in δ^{56}Fe of up to 0.8‰ for magnetite in adjacent layers argue for the absence of significant transport of Fe perpendicular to the layering (Frost et al., 2007). The comparison of Fe isotope compositions of magnetite and siderite from adjacent layers in BIFs from the ~2.5 Ga old Hamersley and Transvaal successions exhibit isotope disequilibrium throughout indicating insufficient Fe isotope exchange between layers (Johnson et al., 2003; Johnson et al., 2008). Predominantly layer-parallel fluid flow is also assumed for the sample investigated for the following reasons, although minor Fe redistribution across layering cannot be excluded: 1) There is no obvious reason why the Fe and Si isotope composition of bulk layers should covary if Fe was redistributed between layers. 2) Adjacent greenish and light layers exhibit significant differences in their Fe concentrations with ~35 and ~10 wt%, respectively. 3) The high abundance of chert, especially in carbonate-chert layers (see Fig. 3 and Table 1) have likely prevented major advection and diffusion perpendicular to layering in this sample. Early silica cementation in BIFs limited the permeability and also restricted the exchange between early diagenetic pore fluids and seawater (Beukes and Gutzmer, 2008). 4) Siderite in adjacent layers shows variable Fe isotope composition. For instance, the LA data reveal δ^{56}Fe of 0.1‰ for siderite in the magnetite-rich layer 5 which is close to the bulk iron carbonate value as siderite is the dominating iron carbonate phase. In the adjacent carbonate layer 6, siderite exhibits δ^{56}Fe of 0.4‰, but the Fe isotope composition of bulk iron carbonate is very similar due to ankerite with a negative signature. The only other reason for differences in siderite from adjacent layers arises from variable proportions of siderite from different growth generations (see Fig. 2) which carry different Fe isotope values.
Therefore bulk layers in the Old Wanderer BIF are assumed to reflect largely primary Si and Fe isotope signatures. During diagenesis, Fe is partitioned within layers into iron carbonate and magnetite, which each provide diagenetic Fe isotope signatures, whereas primary signatures are preserved in bulk layer compositions.

5.3. The significance of zoned magnetite crystals

The fact that magnetite crystals in the Old Wanderer BIF exhibit isotopically heavier rims than cores (Fig. 5) corroborates the diagenetic/metamorphic models discussed above. The observed isotope zonation may also account for the range in δ^{56}Fe determined in individual layers. Similar heterogeneities in magnetite have been found in a BIF from the 3.7 Ga old the Isua Greenstone Belt using secondary ion mass spectrometry (SIMS) (Whitehouse and Fedo, 2007). In Isua, the variability is attributed to isotope reservoir effects in pore waters during diagenesis which is also supported by the data presented here.
Ongoing crystallization of magnetite might have changed successively the Fe isotope composition of the pore water by a Rayleigh distillation process, which in turn influences the Fe isotope composition of magnetite. Several processes can change the pore water composition and cause the observed isotope zonation:
1) Kinetic isotope effects lead to fractionation at rapid precipitation rates if crystal growth is surface-controlled; or fractionation in the fluid phase if crystal growth is transport-controlled. The first effect can be ruled out as an experimental study has shown for the precipitation of hematite from solution that equilibrium conditions are already attained after some days (Skulan et al., 2002), and recrystallization during diagenesis takes place at a time scale of several thousand years (Berner, 1980). More likely is a kinetic effect during the transport of soluble Fe in a fluid phase if advection is negligible and molecular diffusion dominates. Despite the presence of $Fe(II)_{aq}$ as hexaquo complex in aqueous solution which decreases the relative mass differences between isotopes and therefore limits kinetic fractionation effects (Richter et al., 2006), an experimental study of (Rodushkin et al., 2004) postulates a discrimination of dissolved ^{56}Fe relative to ^{54}Fe of -0.3‰ by diffusion.
2) If siderite and magnetite form simultaneously by abiotic reactions and compete for a limited reservoir of $Fe(II)_{aq}$ during diagenesis, their isotope composition might affect each other. Both, siderite and magnetite tend to preferentially incorporate light Fe relative to $Fe(II)_{aq}$ (Table 5) but siderite prefers lighter Fe than magnetite under equilibriums conditions. Hence siderite formation enriches the fluid in heavy Fe in the residual $Fe(II)_{aq}$. This process could be reflected in the magnetite crystals which contain heavy Fe in the rim.
3) An increasing degree of dissolution of ferric (hydr)oxides can produce a temporal evolution towards a heavy residue. Fe isotope studies of reactive Fe(III) in modern anoxic marine sediments have shown such a process due to DIR (Severmann et al., 2006; Staubwasser et al., 2006). There, ferric (hydr)oxides become successively

enriched in heavy Fe as light Fe is preferentially dissolved resulting in a cumulative Fe isotope composition of the pore-water which converges to the initial value of the ferric (hydr)oxides. If magnetite crystallizes from the reaction of ferric (hydr)oxides with $Fe(II)_{aq}$ in the pore water, growing magnetite crystals will accumulate successively heavier Fe with preceding reduction of ferric (hydr)oxide which causes the observed isotope zonation.

6. Conclusions

The evidence provided here for the Old Wanderer BIF suggests that the isotope variations of bulk layers in Fe and Si isotope are largely of primary origin and post-depositional redistribution across layering or recycling to the ocean was minor. Also, the simultaneous precipitation of light carbonate and a heavy iron oxide from seawater can be discounted. Rather, we suggest that both magnetite and iron carbonate are of secondary origin due to the reaction of organic matter with initially precipitated ferric oxyhydroxide either catalyzed by bacteria during early diagenesis, or more likely abiotically during late diagenesis or low-grade metamorphism at temperatures as high as 200°C. Isotope zonation in magnetite is caused by an evolving fluid and reflects dynamic processes during diagenesis. The heavy bulk Fe composition and the light Si composition suggest rapid precipitation events from an episodically recharged hydrothermal fluid. Steady state of Fe and Si was never achieved. The covariance of Fe and Si isotope signatures of bulk layers reflects the upwelling dynamics of hydrothermal-rich waters. The Fe isotope composition of bulk layers therefore indicates variable degrees of partial oxidation in a stratified ocean. The variability of the Si isotope composition might reflect modifications of hydrothermal fluids with distance to the venting site caused by Rayleigh distillation and/or mixing with ambient seawater. The development of layering depends on the relative proportion of organic carbon to ferric (hydr)oxide. This proportion might be governed by the rate of ferric oxyhydroxide precipitation, which is determined by the hydrothermal activity. Periods of low hydrothermal activity are documented by layers with low Fe content which represent conditions, in which an excess of organic carbon has led to complete conversion of ferric (hydr)oxide to carbonate. Layers in which the Fe content is high represents intensive hydrothermal activity and organic carbon was the limiting factor resulting in the additional formation of magnetite.
The analysis of BIF mineral isotope compositions by in situ femtosecond laser ablation analysis provides unprecedented insights into the genetic history of these rocks that cannot be achieved by bulk layer or bulk mineral analysis. Future studies of this kind will allow researchers to decipher the factors controlling BIF formation. For example, variations in iron oxide compositions between layers will allow us to infer temporal variations in the Fe source or in genetic processes. The further development of the laser technique to higher sensitivity and higher spatial resolution will facilitate studies aimed at ascertaining the detailed isotope composition and hence genesis of zoned iron carbonates. In situ analysis is the method of choice for the study of Precambrian iron formations.

Acknowledgements

We acknowledge the support of this study by the DFG, BGR-Hochschulvergabeprogramm, and New Wave Research. T. Oberthuer (BGR) kindly provided sample material. O. Dietrich and W. Hurkuck are thanked for technical support. We thank K. Konhauser for helpful comments on an early version of the manuscript and three reviewers for their constructive suggestions.

References

Anbar A. D., Jarzecki A. A. and Spiro T. G. (2005) Theoretical investigation of iron isotope fractionation between $Fe(H_2O)_6^{3+}$ and $Fe(H_2O)_6^{2+}$: Implications for iron stable isotope geochemistry. *Geochim. Cosmochim. Acta* **69**, 825-837.

Anbar A. D. (2004) Iron stable isotopes: beyond biosignatures. *Earth Planet. Sci. Lett.* **217**, 223-236.

André L., Cardinal D., Alleman L. Y. and Moorbath S. (2006) Silicon isotopes in ~3.8 Ga West Greenland rocks as clues to the Eoarchaean supracrustal Si cycle. *Earth Planet. Sci. Lett.* **245**, 162-173.

Basile-Doelsch I. (2006) Si stable isotopes in the Earth's surface: A review. *J. Geochem. Explor.* **88**, 252-256.

Bau M. and Dulski P. (1996) Distribution of yttrium and rare-earth elements in the Penge and Kuruman iron-formations, Transvaal Supergroup, South Africa. *Precambrian Res.* **79**, 37-55.

Bau M. and Möller P. (1993) Rare earth element systematics of the chemically precipitated component in early Precambrian iron formations and the evolution of the terrestrial atmosphere-hydrosphere-lithosphere system. *Geochim. Cosmochim. Acta* **57**, 2239-2249.

Baur M. E., Hayes J. M., Studley S. A. and Walter M. R. (1985) Millimeter-scale variations of stable isotope abundances in carbonates from Banded Iron-Formations in the Hamersley Group of Western Australia. *Econ. Geol.* **80**, 270-282.

Beard B. L. and Johnson C. M. (2004) Fe isotope variations in the modern and ancient earth and other planetary bodies. In *Geochemistry of non-traditional stable isotopes* (eds. C. M. Johnson, B. L. Beard and F. Albarede). Reviews in Mineralogy & Geochemistry **55**.Mineralogical Soc. America, Washington. pp. 319-357.

Beard B. L., Johnson C. M., Von Damm K. L. and Poulson R. L. (2003) Iron isotope constraints on Fe cycling and mass balance in oxygenated Earth oceans. *Geology* **31**, 629-632.

Becker R. H. and Clayton R. N. (1976) Oxygen isotope study of a Precambrian banded iron-formation, Hamersley Range, Western-Australia. *Geochim. Cosmochim. Acta* **40**, 1153-1165.

Becker R. H. and Clayton R. N. (1972) Carbon isotopic evidence for orgin of banded iron-formation in Western Australia. *Geochim. Cosmochim. Acta* **36**, 577-595.

Berner R. A. (1980) Early diagenesis-A theoretical approach. Princeton University Press, Princeton, New Jersey.

Beukes N. J., Klein C., Kaufman A. J. and Hayes J. M. (1990) Carbonate petrography, kerogen distribution, and carbon and oxygen isotope variations in an early Proterozoic transition from limestone to iron-formation deposition, Transvaal Supergroup, South Africa. *Econ. Geol*. **85**, 663-690.

Bullen T. D., White A. F., Childs C. W., Vivit D. V. and Schulz M. S. (2001) Demonstration of significant abiotic iron isotope fractionation in nature. *Geology* **29**, 699-702.

Canfield D. E. (2005) The early history of atmospheric oxygen: Homage to Robert M. Garrels. *Annu. Rev. Earth Planet. Sci*. **33**, 1-36.

Chang S. B. R., Stolz J. F., Kirschvink J. L. and Awramik S. M. (1989) Biogenic magnetite in stromatolites. 2. Occurrence in ancient sedimentary environments. *Precambrian Res.* **43**, 305-315.

Chmeleff J., Horn I., Steinhoefel G. and von Blanckenburg F. (2008) In situ determination of precise stable Si isotope ratios by UV-femtosecond laser ablation high-resolution multi-collector ICP-MS. *Chem. Geol.* **249**, 155-166.

Croal L. R., Johnson C. M., Beard B. L. and Newman D. K. (2004) Iron isotope fractionation by Fe(II)-oxidizing photoautotrophic bacteria. *Geochim. Cosmochim. Acta* **68**, 1227-1242.

Crosby H. A., Roden E. E., Johnson C. M. and Beard B. L. (2007) The mechanisms of iron isotope fractionation produced during dissimilatory Fe(III) reduction by Shewanella putrefaciens and Geobacter sulfurreducens. *Geobiol.* **5**, 169-189.

Dauphas N., Cates N. L., Mojzsis S. J. and Busigny V. (2007) Identification of chemical sedimentary protoliths using iron isotopes in the > 3750 Ma Nuvvuagittuq supracrustal belt, Canada. *Earth Planet. Sci. Lett*. **254**, 358-376.

Dauphas N. and Rouxel O. (2006) Mass spectrometry and natural variations of iron isotopes. *Mass. Spectrom. Rev.* **25**, 515-550.

Dauphas N., van Zuilen M., Wadhwa M., Davis A. M., Marty B. and Janney P. E. (2004) Clues from Fe isotope variations on the origin of early Archean BIFs from Greenland. *Science* **306**, 2077-2080.

De La Rocha C. L., Brzezinski M. A. and Deniro M. J. (2000) A first look at the distribution of the stable isotopes of silicon in natural waters. *Geochim. Cosmochim. Acta* **64**, 2467-2477.

De La Rocha C. L., Brzezinski M. A. and DeNiro M. J. (1997) Fractionation of silicon isotopes by marine diatoms during biogenic silica formation. *Geochim. Cosmochim. Acta* **61**, 5051-5056.

Ding T., Jiange S., Wan D., Li Y., Li J., Song H., Liu Z. and Yao X. (1996) Silicon Isotope Geochemistry. Geological Publishing House, Beijing, China.

Drever J. I. (1974) Geochemical model for origin of Precambrian Iron Formations. *Geol. Soc. Am. Bull.* **85**, 1099-1106.

Ehrenreich A. and Widdel F. (1994) Anaerobic oxidation of ferrous iron by purple bacteria, a new-type of

phototrophic metabolism. *Appl. Environ. Microbiol.* **60**, 4517-4526.
Ewers W. E. (1983) Chemical factors in the deposition and diagenesis of banded iron-formation. In *Iron-Formation: Facts and Problems* (eds. A. F. Trendall and R. C. Morris). Elsevier, Amsterdam. pp. 491-512.
Ewers W. E. and Morris R. C. (1981) Studies of the Dales Gorge member of the Brockman iron formation, Western Australia. *Econ. Geol.* **76**, 1929-1953.
Fedo C. M., Whitehouse M. J. and Kamber B. S. (2006) Geological constraints on detecting the earliest life on Earth: A perspective from the Early Archaean (older than 3.7 Gyr) of southwest Greenland. *Phil. Trans. R. Soc. (London) B* **361**, 851-867.
Foster R. P. and Gilligan J. M. (1987) Archean iron-formation and gold mineralization in Zimbabwe. In *Precambrian iron-formation* (eds. P. W. Uitterdijk Appel and G. L. Laberge). Theophrastus Publications, Athen. pp. 635-674.
Frost C. D., von Blanckenburg F., Schoenberg R., Frost B. R. and Swapp S. M. (2007) Preservation of Fe isotope heterogeneities during diagenesis and metamorphism of banded iron formation. *Contrib. Mineral. Petrol.* **153**, 211-235.
Goodwin A. M., Monster J. and Thode H. G. (1976) Carbon and Sulfar isotope abundances in Archean iron-formations and early Precambrian Life. *Econ. Geol.* **71**, 870-891.
Han T. (1978) Microstructures of magnetite as guide to its origin in some Precambrian iron formations. *Fortschr. Mineral.* **56**, 105-142.
Holland H. D. (2006) The oxygenation of the atmosphere and oceans. *Phil. Trans. R. Soc. (London) B* **361**, 903-915.
Holland H. D. (1973) Ocean - possible source of iron in iron-formations. *Econ. Geol.* **68**, 1169-1172.
Horn I. and von Blanckenburg F. (2007) Investigation on elemental and isotopic fractionation during 196 nm femtosecond laser ablation multiple collector inductively coupled plasma mass spectrometry. *Spectrochim. Acta Part B* **62**, 410-422.
Horn I., von Blanckenburg F., Schoenberg R., Steinhoefel G. and Markl G. (2006) In situ iron isotope ratio determination using UV-femtosecond laser ablation with application to hydrothermal ore formation processes. *Geochim. Cosmochim. Acta* **70**, 3677-3688.
Jiang S. Y., Ding T. P., Wan D. F. and Li Y. H. (1993) Silicon isotopic compositions of Archean banded Si-Fe Formation (BIF) in the Gongchangling Ore Deposit, Liaoning-Province, China. *Chin. Sci. Bull. (Series B)* **36**, 482-489.
Johnson C. M., Beard B. L., Klein C., Beukes N. J. and Roden E. E. (2008) Iron isotopes constrain biologic and abiologic processes in banded iron formation genesis. *Geochim. Cosmochim. Acta* **72**, 151-169.
Johnson C. M. and Beard B. L. (2006) Fe isotopes: An emerging technique for understanding modern and ancient biogeochemical cycles. *GSA Today* **16**, 4-10.
Johnson C. M., Roden E. E., Welch S. A. and Beard B. L. (2005) Experimental constraints on Fe isotope fractionation during magnetite and Fe carbonate formation coupled to dissimilatory hydrous ferric oxide reduction. *Geochim. Cosmochim. Acta* **69**, 963-993.
Johnson C. M., Beard B. L., Beukes N. J., Klein C. and O'Leary J. M. (2003) Ancient geochemical cycling in the Earth as inferred from Fe isotope studies of banded iron formations from the Transvaal Craton. *Contrib. Mineral. Petrol.* **144**, 523-547.
Johnson C. M., Skulan J. L., Beard B. L., Sun H., Nealson K. H. and Braterman P. S. (2002) Isotopic fractionation between Fe(III) and Fe(II) in aqueous solutions. *Earth Planet. Sci. Lett.* **195**, 141-153.
Kappler A., Pasquero C., Konhauser K. O. and Newman D. K. (2005) Deposition of banded iron formations by anoxygenic phototrophic Fe(II)-oxidizing bacteria. *Geology* **33**, 865-868.
Karlin R., Lyle M. and Heath G. R. (1987) Authigenic magnetite formation in suboxic marine sediments. *Nature* **326**, 490-493.
Kaufman A. J., Johnston D. T., Farquhar J., Masterson A. L., Lyons T. W., Bates S., Anbar A. D., Arnold G. L., Garvin J. and Buick R. (2007) Late Archean biospheric oxygenation and atmospheric evolution. *Science* **317**, 1900-1903.
Kaufman A. J., Hayes J. M. and Klein C. (1990) Primary and diagenetic controls of isotopic compositions of iron- formation carbonates. *Geochim. Cosmochim. Acta* **54**, 3461-3473.
Klein C. (2005) Some Precambrian banded iron-formations (BIFs) from around the world: Their age, geologic setting, mineralogy, metamorphism, geochemistry, and origin. *Am. Mineral.* **90**, 1473-1499.
Klein C. and Beukes N. J. (1989) Geochemistry and sedimentology of a facies transition from limestone to iron-formation deposition in the early Proterozoic Transvaal Supergroup, South Africa. *Econ. Geol.* **84**, 1733-1774.
Konhauser K., Amskold L., Lalonde S., Posth N., Kappler A. and Anbar A. (2007) Decoupling photochemical Fe(II) oxidation from shallow-water BIF deposition. *Earth Planet. Sci. Lett.* **258**, 87-100.
Konhauser K. O., Newman D. K. and Kappler A. (2005) The potential significance of microbial Fe(III) reduction during deposition of Precambrian banded iron formations. *Geobiol.* **3**, 167-177.
Konhauser K. O., Hamade T., Raiswell R., Morris R. C., Ferris F. G., Southam G. and Canfield D. E. (2002)

Could bacteria have formed the Precambrian banded iron formations? *Geology* **30**, 1079-1082.
Konhauser K. O. (1998) Diversity of bacterial iron mineralization. *Earth. Sci. Rev.* **43**, 91-121.
Lovley D. (1997) Microbial Fe(III) reduction in subsurface environments. *FEMS Microbiol. Rev.* **20**, 305-313.
Lovley D. R. (1990) Magnetite formation during microbial dissimilatory iron reduction. In *Iron biominerals* (eds. R. B. Frankel and R. P. Blakemore), Plenum Press, New York, pp. 151–166.
Lovley D. R. (1991) Dissimilatory Fe(III) and Mn(IV) reduction. *Microbiol. Rev*. **55**, 259-287.
Lovley D. R., Stolz J. F., Nord Jr G. L. and Phillips E. J. P. (1987) Anaerobic production of magnetite by a dissimilatory iron-reducing microorganism. *Nature* **330**, 252-254.
Maliva R. G., Knoll A. H. and Simonson B. M. (2005) Secular change in the Precambrian silica cycle: Insights from chert petrology. *Geol. Soc. Am. Bull.* **117**, 835-845.
Mandernack, K.W., Bazylinski, D.A., Shanks, W.C. and Bullen, T.D. (1999) Oxygen and iron isotope studies of magnetite produced by magnetotactic bacteria. *Science* **285**, 1892-1896
Mineev S. D., Polyakov V. B. and Permyakov Y. V. (2007) Equilibrium iron isotope fractionation factors for magnetite from Mössbauer spectroscopy and inelastic nuclear resonant X-ray scattering data. *Geochim. Cosmochim. Acta* **71**, A669 (abstr.).
Mojzsis S. J., Arrhenius G., McKeegan K. D., Harrison T. M., Nutman A. P. and Friend C. R. L. (1996) Evidence for life on Earth before 3,800 million years ago. *Nature* **384**, 55-59.
Moorbath S., Taylor P. N., Orpen J. L., Treloar P. and Wilson J. F. (1987) First direct radiometric dating of Archean stromatolitic limestone. *Nature* **326**, 865-867.
Morris R. C. (1993) Genetic modelling for banded iron-formation of the Hamersley Group, Pilbara Craton, Western Australia. *Precambrian Res.* **60**, 243-286.
Oberthuer T., Saager R. and Tomschi H. (1990) Geological, mineralogical and geochemical aspects of archean banded iron-formation-hosted gold deposits: some examples from southern Africa. *Miner. Deposita* **25**, 125-135.
Ohmoto H. (2003) Nonredox transformations of magnetite-hematite in hydrothermal systems. *Econ. Geol.* **98**, 157-161.
Perry E. C. and Lefticariu L. (2003) Formation and geochemistry of Precambrian cherts. In *Treatise on Geochemistry* (ed. F. T. Mackenzie). Elsevier, Amsterdam. pp. 99-113.
Perry E. C., Ahmad S. N. and Swulius T. M. (1978) Oxygen isotope composition of 3,800 my old metamorphosed chert and iron formation from Isukasia, West-Greenland. *J. Geol.* **86**, 223-239.
Perry E. C., Tan F. C. and Morey G. B. (1973) Geology and stable isotope geochemistry of Biwabik iron formation, northern Minnesota. *Econ. Geol.* **68**, 1110-1125.
Pickard A. L. (2002) SHRIMP U-Pb zircon ages of tuffaceous mudrocks in the Brockman Iron Formation of Hamersley Range, Western Australia. *Aust. J. Earth Sci.* **49**, 491-507.
Pickard A. L. (2003) SHRIMP U-Pb zircon ages for the Palaeoproterozoic Kuruman Iron Formation, Northern Cape Province, South Africa: Evidence for simultaneous BIF deposition on Kaapvaal and Pilbara Cratons. *Precambrian Res.* **125**, 275-315.
Polyakov V. B., Clayton R. N., Horita J. and Mineev S. D. (2007) Equilibrium iron isotope fractionation factors of minerals: Reevaluation from the data of nuclear inelastic resonant X-ray scattering and Mössbauer spectroscopy. *Geochim. Cosmochim. Acta* **71**, 3833-3846.
Polyakov V. B. and Mineev S. D. (2000) The use of Mössbauer spectroscopy in stable isotope geochemistry. *Geochim. Cosmochim. Acta* **64**, 849-865.
Prendergast M. D. (2004) The Bulawayan Supergroup: A late Archaean passive margin-related large igneous province in the Zimbabwe craton. *J. Geol. Soc. London* **161**, 431-445.
Richter F. M., Mendybaev R. A., Christensen J. N., Hutcheon I. D., Williams R. W., Sturchio N. C. and Beloso A. D. (2006) Kinetic isotopic fractionation during diffusion of ionic species in water. *Geochim. Cosmochim. Acta* **70**, 277-289.
Robert F. and Chaussidon M. (2006) A palaeotemperature curve for the Precambrian oceans based on silicon isotopes in cherts. *Science* **443**, 969-972.
Roden, E E Sobolev, D Glazer, B Luther, G W (2004) Potential for microscale bacterial Fe redox cycling at the aerobic-anaerobic interface. *Geomicrobiol. J.* **21**, 391.
Rodushkin I., Stenberg A., Andreń H., Malinovsky D. and Baxter D. C. (2004) Isotopic Fractionation during Diffusion of Transition Metal Ions in Solution. *Anal. Chem.* **76**, 2148-2151.
Rouxel O. J., Bekker A. and Edwards K. J. (2005) Iron isotope constraints on the Archean and Paleoproterozoic ocean redox state. *Science* **307**, 1088-1091.
Schoenberg R. and von Blanckenburg F. (2005) An assessment of the accuracy of stable Fe isotope ratio measurements on samples with organic and inorganic matrices by high-resolution multicollector ICP-MS. *Int. J. Mass Spectrom.* **242**, 257-272.
Severmann S., Johnson C. M., Beard B. L. and McManus J. (2006) The effect of early diagenesis on the Fe isotope compositions of porewaters and authigenic minerals in continental margin sediments. *Geochim. Cosmochim. Acta* **70**, 2006-2022.
Severmann S., Johnson C. M., Beard B. L., German C. R., Edmonds H. N., Chiba H. and Green D. R. H. (2004)

The effect of plume processes on the Fe isotope composition of hydrothermally derived Fe in the deep ocean as inferred from the Rainbow vent site, Mid-Atlantic Ridge, 36 degrees 14' N. *Earth Planet. Sci. Lett.* **225**, 63-76.

Siever R. (1992) The silica cycle in the Precambrian. *Geochim. Cosmochim. Acta* **56**, 3265-3272

Sharma M., Polizzotto M. and Anbar A. D. (2001) Iron isotopes in hot springs along the Juan de Fuca Ridge. *Earth Planet. Sci. Lett.* **194**, 39-51.

Skulan J. L., Beard B. L. and Johnson C. M. (2002) Kinetic and equilibrium Fe isotope fractionation between aqueous Fe(III) and hematite. *Geochim. Cosmochim. Acta* **66**, 2995-3015.

Staubwasser M., von Blanckenburg F. and Schoenberg R. (2006) Iron isotopes in the early marine diagenetic iron cycle. *Geology* **34**, 629-632.

Sumner D. Y. (1997) Carbonate precipitation and oxygen stratification in late Archean seawater as deduced from facies and stratigraphy of the Gamohaan and Frisco formations, Transvaal Supergroup, South Africa. *Am. J. Sci.* **297**, 455-487.

Trendall A. F., Compston W., Nelson D. R., De Laeter J. R. and Bennett V. C. (2004) SHRIMP zircon ages constraining the depositional chronology of the Hamersley Group, Western Australia. *Aust. J. Earth Sci.* **51**, 621-644.

Trendall A. (2002) The signifcance of iron-formation in the Precambrian stratigraphic record. In *Precambrian Sedimentary Environments: A Modern Approach to Depositional Systems.* Special Publication International Association of Sedimentologists **33**, 33-66.

Tyndale-Biscoe M. A. (1949) The Geology of the Country around Gwelo. Southern Rhodesia Geological Survey, Bulletin No. 39. Reprinted by the Government Printer, Salisbury, 1972.

van den Boorn S. H. J. M., van Bergen M. J., Nijman W. and Vroon P. Z. (2007) Dual role of seawater and hydrothermal fluids in Early Archean chert formation: Evidence from silicon isotopes. *Geology* **35**, 939-942.

Vargas M., Kashefi K., Blunt-Harris E. and Lovley D. (1998) Microbiological evidence for Fe(III) reduction on early earth. *Nature* **395**, 65-67.

Valaas Hyslop E., Valley J. W., Johnson C. M. and Beard B. L. (2008) The effects of metamorphism on O and Fe isotope compositions in the Biwabik iron-formation, northern Minnesota. *Contrib. Mineral. Petrol.* **155**, 313-328.

von Blanckenburg F., Mamberti M., Schoenberg R., Kamber B. S. and Webb G. E. (2008) The iron isotope composition of microbial carbonate. *Chem. Geol.* **249**, 113-128.

Walker J. C. G. (1984) Suboxic diagenesis in banded iron formations. *Nature* **309**, 340-342.

Welch S. A., Beard B. L., Johnson C. M. and Braterman P. S. (2003) Kinetic and equilibrium Fe isotope fractionation between aqueous Fe(II) and Fe(III). *Geochim. Cosmochim. Acta* **67**, 4231-4250.

Whitehouse M. J. and Fedo C. M. (2007) Microscale heterogeneity of Fe isotopes in > 3.71 Ga banded iron formation from the Isua Greenstone Belt, Southwest Greenland. *Geology* **35**, 719-722.

Wiesli R. A., Beard B. L. and Johnson C. M. (2004) Experimental determination of Fe isotope fractionation between aqueous Fe(II), siderite and "green rust" in abiotic systems. *Chem. Geol.* **211**, 343-362.

Wilson J. F., Nesbitt R. W. and Fanning C. M. (1995) Zircon geochronology of Archaean felsic sequences in the Zimbabwe craton: a revision of greenstone stratigraphy and a model for crustal growth. In *Early Precambrian Processes* (eds. M. P. Coward and A. C. Reis) Geological Society, London, pp. 109-126 (Special Publications 95).

Ziegler K., Chadwick O. A., Brzezinski M. A. and Kelly E. F. (2005) Natural variations of δ^{30}Si ratios during progressive basalt weathering, Hawaiian Islands. *Geochim. Cosmochim. Acta* **69**, 4597-4610.

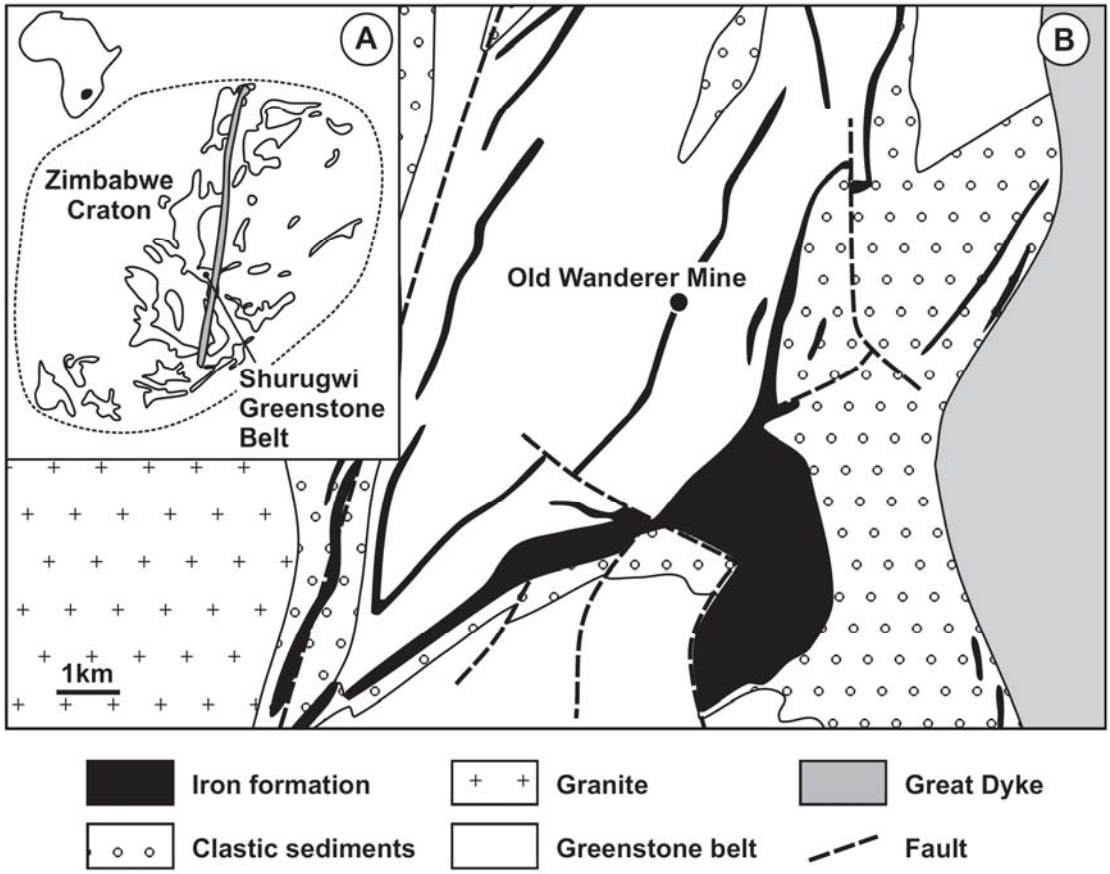

Figure 1: Simplified geological map of the Shurugwi Greenstone Belt. **A)** Greenstone belts (white) and Great Dyke (grey) within the Archean Zimbabwe Craton (modified after Oberthuer et al., 1990). **B)** Part of the *ca.* 2.7 Ga old Shurugwi Greenstone Belt (modified after Tyndale-Biscoe, 1949). Rocks of the greenstone belt include epidiorite, basaltic schist and serpentine. The Wanderer Formation consists of banded iron formation and clastic rocks including conglomerate, grit, quartzite and phyllitic schist. The investigated sample was collected in the area of the Old Wanderer Mine.

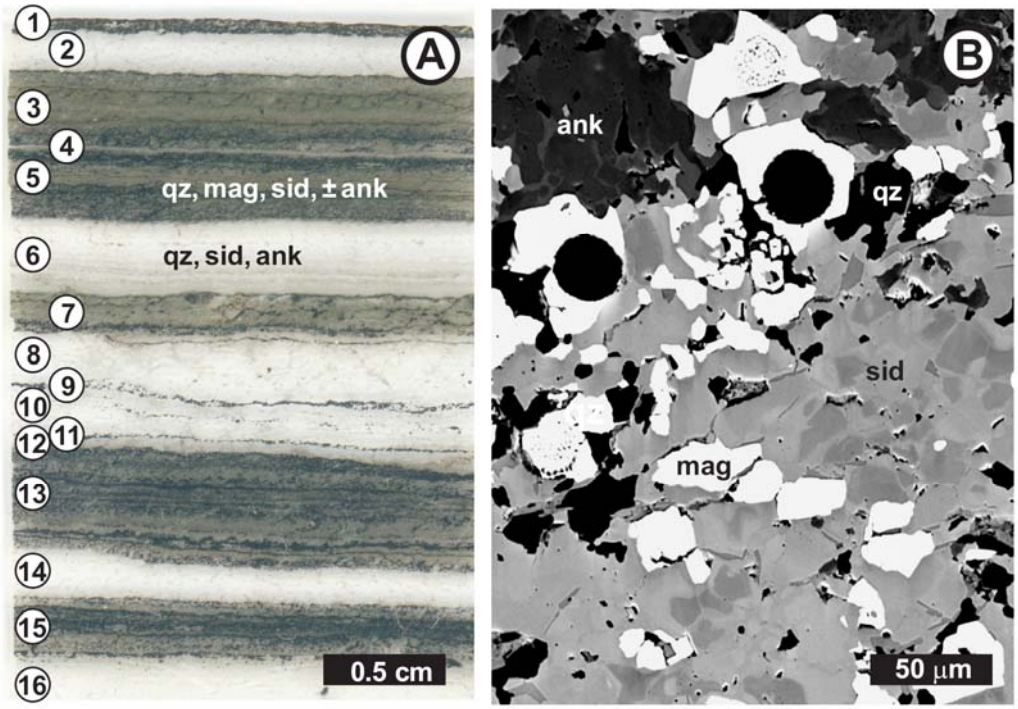

Figure 2: Photograph and backscattered electron (BSE) image of the Old Wanderer BIF from the *ca.* 2.7 Ga old Shurugwi Greenstone Belt with mag=magnetite, sid=siderite, ank=ankerite and qz=chert. **A)** The investigated thin section exhibits alternating carbonate-chert and magnetite-carbonate-chert layers. **B)** The BSE image shows laser ablation craters in magnetite crystals. Both types of iron carbonates exhibit chemically zoned crystals indicating a complex growth history. Cores of irregular shape show distinct transitions to interlocked overgrowths which differ in Mg substitution.

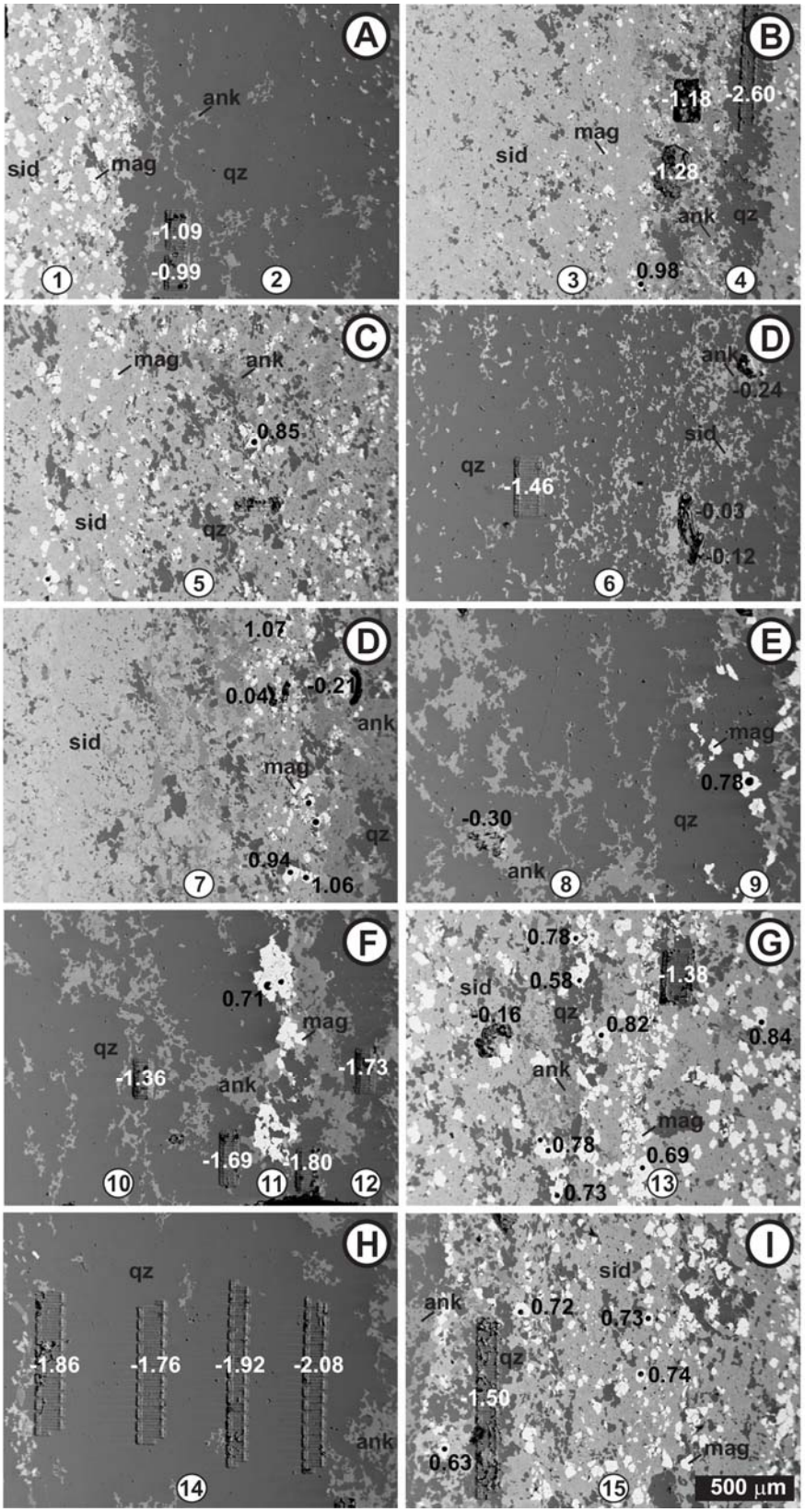

Figure 3: BSE images of representative sections of the investigated layers with mag=magnetite, sid=siderite, ank=ankerite and qz=chert. The numbering of the layers corresponds to Figure 2a. Fe isotope analyses in magnetite (spots) and in Fe carbonates (short line scans) are labelled with δ^{56}Fe values in ‰ (black numbers). Si isotope analyses in chert (rasters) are indicated with δ^{30}Si values in ‰ (white numbers).

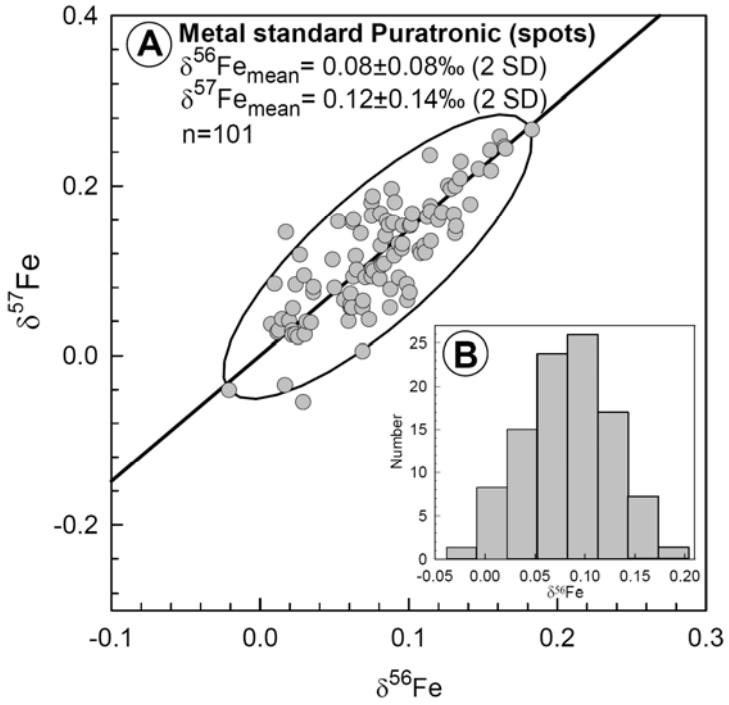

Figure 4: Reproducibility of Fe isotope spot analyses by LA-ICP-MS. **A)** The metal standard Puratronic was repeatedly measured against the reference material IRMM-014 over a course of about 9 months and plotted in a three isotope diagram. The error ellipse indicates the 95% confidence level of the Puratronic data. **B)** Histogram of Puratronic data shows a Gaussian distribution.

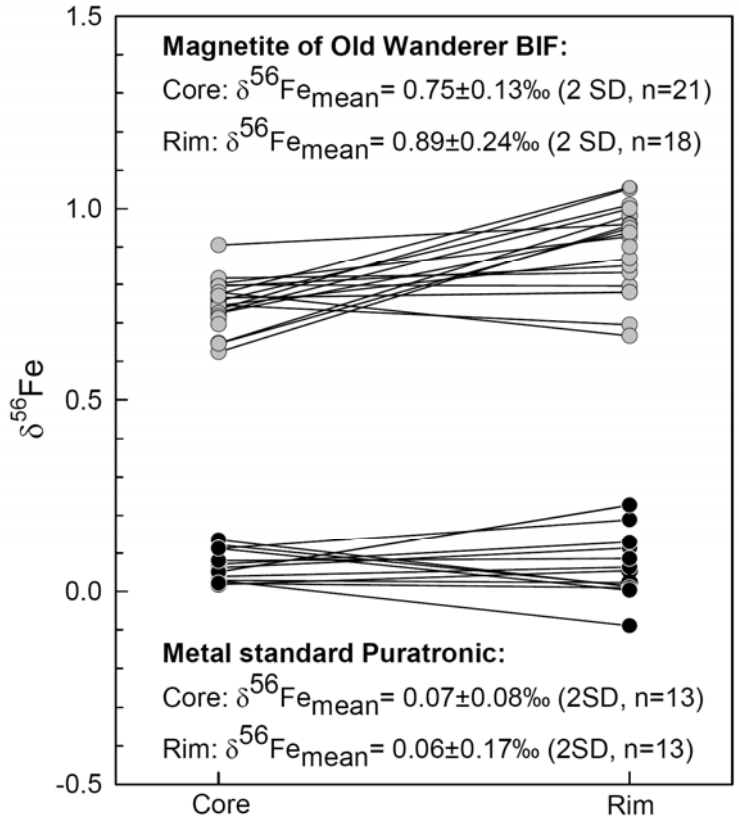

Figure 5: Fe isotope zonation in magnetite crystals in the Old Wanderer BIF. Corresponding pairs of core-rim analysis in layer 13 (Fig. 2a) show that magnetite crystals tend to be heavier in their Fe isotope composition towards the rim. Considering all data the relative mean difference between core and rim is 0.14‰ in δ^{56}Fe. To verify this method, the same experiment was carried out on the homogeneous metal standard Puratronic. Here the inner spot analyses (=core) are identical with the outer spot analyses (=rim) within the analytical precision.

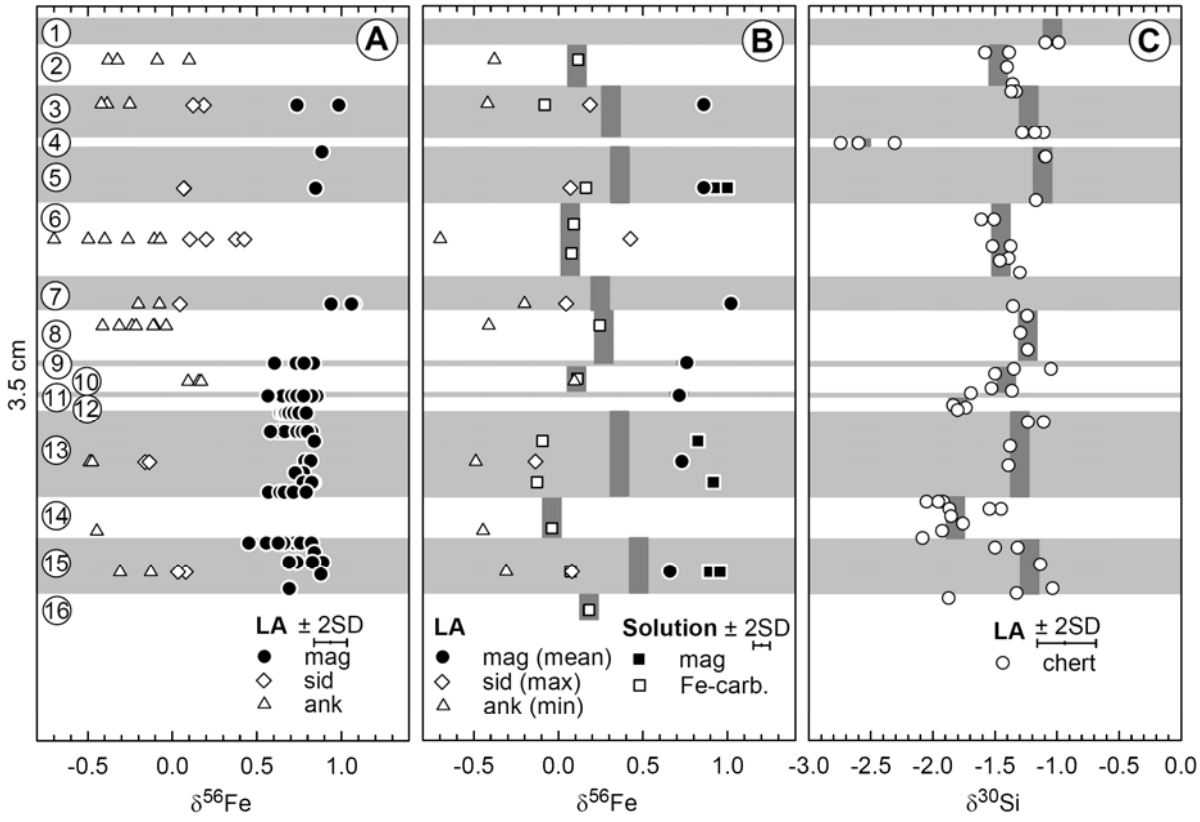

Figure 6: Fe and Si isotope variations in the Old Wanderer BIF within a section of 3.5 cm. The numbering of layers corresponds to Figure 2a. Carbonate layers consists of siderite, ankerite and chert (in white), whereas magnetite-rich layers are mainly composed of magnetite, siderite and chert (in grey). **A)** Fe isotope data for magnetite, siderite and ankerite obtained by LA-ICP-MS. Single magnetite crystals were investigated by LA spot analyses revealing significant variations in the Fe isotope composition. Siderite and ankerite were analysed by LA using the raster mode. The variation in the Fe isotope composition of siderite and ankerite are largely attributed to variable mixing proportions of these end member minerals. The lowest and the highest $\delta^{56}Fe$ values represent the best estimates of ankerite and siderite end member composition, respectively. **B)** Fe isotope composition of bulk mineral separates obtained by solution ICP-MS and summary of Fe isotope data obtained by LA-ICP-MS. The estimated Fe isotope composition of bulk layers is indicated by vertical bars. **C)** Si isotope composition of chert obtained by LA-ICP-MS using raster mode. Average Si isotope composition of layers is indicated by vertical bars. The Fe and Si isotope compositions of bulk layers covary (correlation factor=0.71, 95% confidence level).

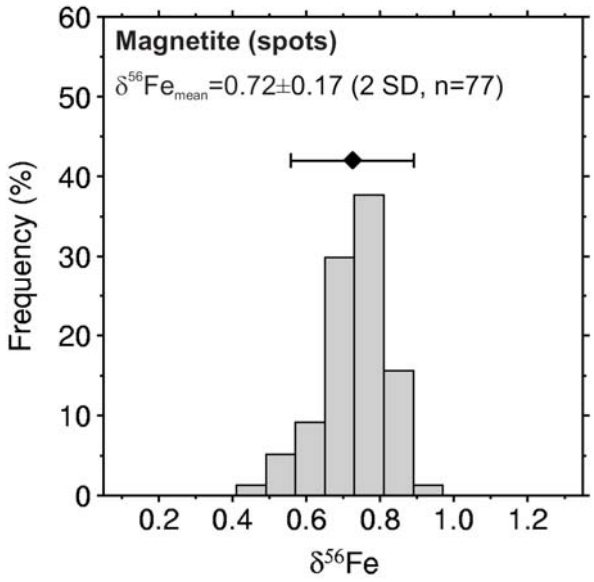

Figure 7: Histograms of Fe isotope data of magnetite obtained by LA spot analyses. The population exhibits a Gaussian distribution. The standard deviation differs significantly from the external reproducibility (error bar) indicating true heterogeneity in the Fe isotope composition on a sub-millimeter scale.

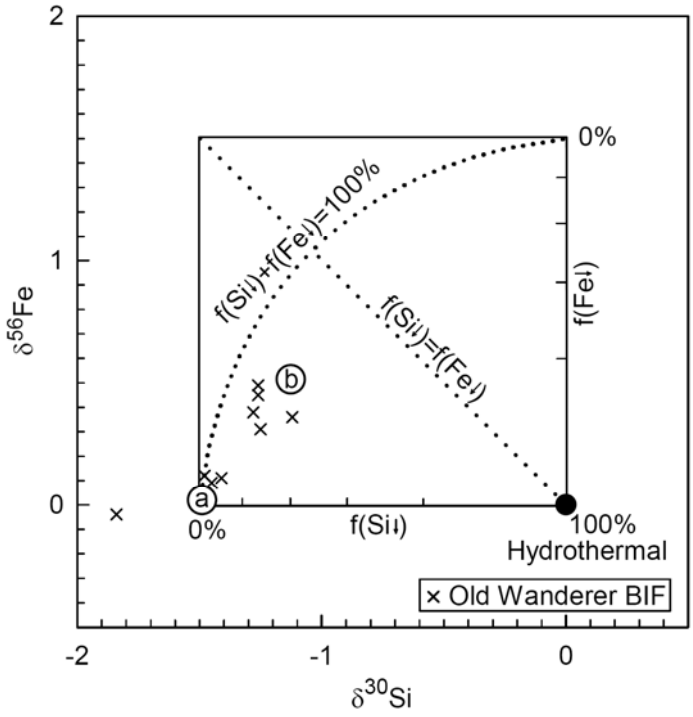

Figure 8: Conceptual model of the variability in $\delta^{30}Si$ and $\delta^{56}Fe$ for the initial precipitates, silica and ferric oxyhydroxide depending on the precipitated fraction f. A hypothetical hydrothermal solution is emanated with $\delta^{56}Fe$ and $\delta^{30}Si$ of 0‰, respectively. Precipitation from this fluid takes place with Fe(III) that is 1.5‰ heavier (through oxidation and ferric oxyhydroxide precipitation, Table 5), and SiO_2 (from oversaturation of seawater with Si) that is 1.5‰ lighter. Two opposing scenarios can be envisaged. In the first case, the hydrothermal influx and the depositional output have the same isotope compositions of 0‰ which can be attained either by steady state conditions or 100% precipitation of the dissolved Fe and Si. In the second case, precipitation of small fractions from seawater with a hydrothermal signature results in isotope compositions reflecting the fractionation factors of -1.5‰ in $\delta^{30}Si$ and 1.5‰ in $\delta^{56}Fe$. The diagonal line illustrates the isotope evolution by Rayleigh distillation for precipitating equal fractions of dissolved Si and Fe, and the axes of the inset indicate the fractions of Fe and Si precipitated. The data of bulk layers of the Old Wanderer BIF (only $\delta^{30}Si$ - $\delta^{56}Fe$ pairs are shown) plot below this line indicating low degrees of Si precipitation (1-40%) at high degrees of Fe precipitation (85-100%) but not steady state conditions. The correlation of the data roughly follows a curve of opposite fractions of cumulative precipitated Si and Fe (f(Si↓)+f(Fe↓)=100%). A possible scenario for the end members of the data indicated by a) and b) is sketched in Figure 9a und b, respectively.

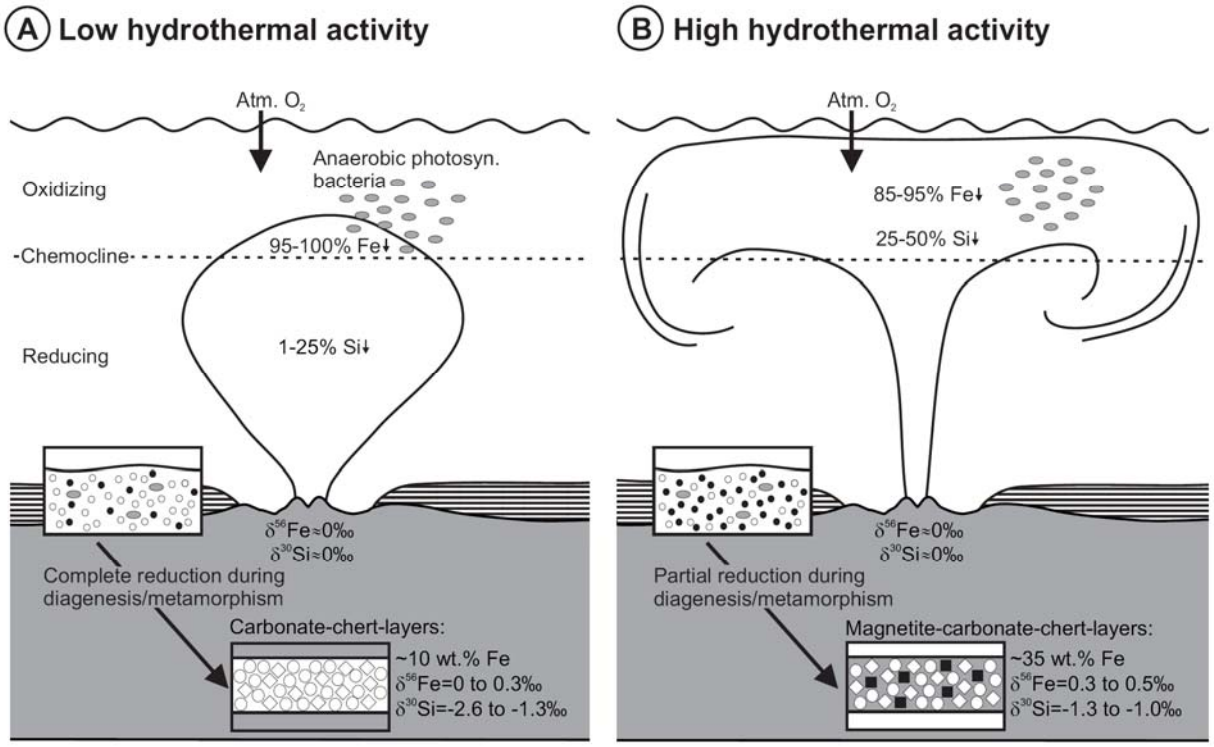

Figure 9: Scenario of episodic recharge and precipitation events by pulses of hydrothermal fluids and the origin of BIF layering. Silica (small open cycles) is likely to precipitate from the entire water column, whereas the formation of ferric oxyhydroxide (small black cycles) is restricted to the oxidizing surface. Magnetite (black squares) and iron carbonate (open diamonds) are diagenetic products of reduction of initial precipitated ferric oxyhydroxide by oxidizing of organic matter (greys ellipsoids); silica consolidates to chert (large open cycles).

A) Low spatial expansion of the hydrothermal plume leads to layers which have low $\delta^{30}Si$ and $\delta^{56}Fe$ values at low Fe contents corresponding to the data marked with a) in Figure 8. Silica precipitates from a pristine fluid near the venting site and represents a small fraction of the dissolved Si resulting in strongly negative $\delta^{30}Si$ values. The supply of $Fe(II)_{aq}$ into the oxidizing upper water column is limited causing near-complete oxidation at low rates of ferric oxyhydroxide precipitation with $\delta^{56}Fe$ values close to the hydrothermal signature, i.e. 0‰. Silica, ferric oxyhydroxide and organic matter are deposited and buried together at the seafloor. The low quantity of ferric oxyhydroxide deposition promotes conditions of organic carbon excess which triggers complete reduction of Fe(III) and conversion to iron carbonate during diagenesis/metamorphism. For example, one mole of organic carbon can reduce eight moles of ferric oxyhdroxide (e.g. Lovley, 1990). These periods are documented by carbonate-chert layers which show low $\delta^{30}Si$ and $\delta^{56}Fe$ values at low Fe contents.

B) Expansion and upwelling of the hydrothermal plume results in layers with higher $\delta^{30}Si$ and $\delta^{56}Fe$ values at high Fe contents which is marked with b) in Figure 8. Now, silica precipitates predominately from a fluid that has previously been modified by ongoing precipitation of isotopically light products with distance to the venting site or by mixing with ambient seawater with a strong positive isotope composition. Both shift the isotope signature towards higher values (André et al., 2006; van den Boorn et al., 2007). The supply of large quantities of $Fe(II)_{aq}$ into the oxidizing zone triggers partial oxidation as the oxidant becomes the limiting factor resulting in high rates of ferric oxyhydroxide precipitation with significantly positive $\delta^{56}Fe$ values. The large quantities of ferric oxyhydroxide deposition trigger partial reduction of Fe(III) as the organic carbon now is the factor limiting reduction resulting in the formation of iron carbonate and magnetite. After diagenesis, these periods are represented by magnetite-carbonate-chert layers which exhibit significant positive $\delta^{56}Fe$ values and moderately negative $\delta^{30}Si$ values at high Fe contents.

Table 1
Average chemical composition (in weight % ± 1 SD) for Fe-bearing mineral phases of the Old Wanderer BIF determined by electron microprobe

Mineral	mag (n=4)	sid 1 (n=6)	sid 2 (n=4)	ank 1 (n=4)	ank 2 (n=5)
SiO_2	0.87 ± 0.46	0.04 ± 0.03	0.04 ± 0.04	0.04 ± 0.05	0.04 ± 0.03
TiO_2	0.02 ± 0.02	0	0	0.01 ± 0.02	0.01 ± 0.01
Al_2O_3	0.06 ± 0.03	0	0.01 ± 0.01	0	0
Fe_2O_3	67.03 ± 1.24	0	0	0	0
FeO	32.18 ± 0.55	56.67 ± 1.45	50.8 ± 0.94	24.54 ± 1.71	19.96 ± 1.11
MnO	0.03 ± 0.05	0.45 ± 0.22	1.21 ± 0.27	0.54 ± 0.22	0.87 ± 0.21
MgO	0	3.08 ± 1.01	7.89 ± 1.11	5.11 ± 0.74	8.26 ± 0.76
CaO	0.03 ± 0.03	0.4 ± 0.16	0.35 ± 0.08	25.65 ± 0.13	26.07 ± 0.44
Na_2O	0.01 ± 0.02	0.02 ± 0.02	0.02 ± 0.02	0.01 ± 0.02	0.03 ± 0.02
K_2O	0.01 ± 0.01	0.01 ± 0.01	0.01 ± 0.01	0.01 ± 0.01	0
Total	100.24 ± 0.45	60.68 ± 0.35	60.34 ± 0.65	55.91 ± 0.78	55.24 ± 0.33

Siderite and ankerite appear each in two distinct chemical compositions with variable proportions of Mg and Fe, as indicated by sid1 & sid2 and ank1 & ank2, respectively.

Table 2
Fe isotope data obtained by LA-ICP-MS and solution ICP-MS

LA-ICP-MS							Solution ICP-MS			
Layer	Mineral		$\delta^{56}Fe_{mean}$	$\delta^{56}Fe_{em}$	2 SD	no. of analyses	Layer	Mineral		$\delta^{56}Fe$
1	ank		-0.17	-0.38	0.44	4	2	sid+ank		0.12
3	mag		0.86		0.35	2	3	sid±ank		-0.08
	ank		-0.35	-0.42	0.18	3	5	mag		1.00
	sid		0.15	0.19	0.09	2				0.92
5	mag		0.86		0.05	2		sid±ank		0.16
	sid		0.07	0.07	0.01	2				
6	ank		-0.34	-0.70	0.48	6	6	sid+ank	a	0.09
	sid		0.28	0.43	0.30	4			b	0.08
7	mag		1.02		0.15	3	8	sid+ank		0.25
	ank		-0.14	-0.20	0.18	2	10	sid+ank		0.11
	sid		0.04			1	13	mag	a	0.82
8	ank		-0.20	-0.41	0.26	7			b	0.92
9	mag		0.76		0.15	7		sid±ank	a	-0.10
10	ank		0.14	0.09	0.08	3			b	-0.13
11	mag		0.71		0.21	9	14	sid+ank		-0.04
13	mag	a	0.71		0.08	17	15	mag		0.89
		b	0.73		0.16	11				0.96
		c	0.67		0.17	5		sid±ank		0.07
		total	0.73		0.14	41	16	sid+ank		0.18
	ank		-0.48	-0.49	0.02	3				
	sid		-0.15	-0.14	0.04	2				
14	ank		-0.45			1				
15	mag	a	0.66		0.18	11				
		b	0.77		0.16	5				
		total	0.71		0.22	20				
	ank		-0.22	-0.31	0.26	2				
	sid		0.06	0.08	0.06	2				

The numbering of layers corresponds to Figure 4, letters refer to different stratigraphic levels within layers. LA-ICP-MS data are presented as mean values, but all data are plotted in Figures 4 and 5. 2 SD refers to multiple analyses (n). In addition, we provide potential end member ratios ($\delta^{56}Fe_{em}$) for ankerite and siderite, respectively. The minimal value represents the endmember composition of ankerite, whereas the maximal value corresponds best to the end member composition of siderite.

Table 3
Estimated modal abundances and Fe and Si isotope composition of bulk layers.

layer	qz	mag	sid	ank	δ^{56}Fe	δ^{30}Si
1	30	40	30	0		-1.04
2	90	0	6	4	0.12	-1.48
3	15	10	72	3	0.31	-1.25
4	100	0	0	0		-2.55
5	15	15	65	5	0.36	-1.12
6	70	0	15	15	0.09	-1.45
7	15	10	65	10	0.22	-1.35
8	70	0	0	30	0.25	-1.26
9	0	100	0	0	0.76	
10	70	0	5	25	0.11	-1.41
11	0	100	0	0	0.71	
12	70	0	0	30		-1.79
13	30	20	45	5	0.30	-1.28
14	90	0	3	7	-0.04	-1.84
15	30	20	45	5	0.43	-1.26
16	90	0	5	5	0.18	-1.87

The Fe isotope composition of bulk layers is calculated from Fe isotope data of the major Fe-bearing mineral phases, their estimated modal abundances, and Fe contents. The Si isotope composition of bulk layers is inferred from multiple analyses of chert (see Table 4). The δ^{56}Fe and δ^{30}Si values of bulk layers are covariant with a correlation factor of 0.74, significant at the confidence level of 5%. Numbering of layers corresponds to Figure 4.

Table 4
Si isotope data of chert obtained by LA-ICP-MS

Layer		δ^{30}Si	2 SD	Layer		δ^{30}Si	2 SD
1		-1.09		10		-1.05	
		-0.99				-1.35	
	total	-1.04	0.15			-1.50	
						-1.53	
2		-1.39				-1.36	
		-1.58				-1.69	
		-1.39			total	-1.41	0.44
		-1.58					
	total	-1.48	0.22	12		-1.84	
						-1.73	
3		-1.33				-1.80	
		-1.37			total	-1.79	0.10
		-1.28					
		-1.11		13		-1.11	
		-1.18				-1.23	
	total	-1.25	0.22			-1.38	
						-1.39	
4		-2.74			total	-1.28	0.27
		-2.31					
		-2.60		14		-1.45	
	total	-2.55	0.44			-1.54	
						-2.05	
5		-1.10				-1.92	
		-1.09				-1.96	
		-1.17				-1.87	
	total	-1.12	0.09			-1.85	
						-1.76	
6		-1.51				-1.92	
		-1.61				-2.08	
		-1.37			total	-1.84	0.41
		-1.52					
		-1.39		15		-1.32	
		-1.46				-1.50	
		-1.30				-1.13	
	total	-1.45	0.21			-1.33	
						-1.04	
7		-1.35			total	-1.26	0.32
8		-1.24		16		-1.87	
		-1.29					
		-1.24					
	total	-1.26	0.07				

The numbering of layers corresponds to Figure 4.

Table 5
Fe isotope fractionation factors

Reactant	Product	Condition	$\Delta^{56}Fe_{Product-Reactant}$ (‰)		Reference
Experimental studies			**T= 22°C**	**T= 98°C**	
$Fe(II)_{aq}$	$Fe(III)_{aq}$	equilibrium	+2.8 to +3.0		Johnson et al. (2002), Welch et al. (2003)
$Fe(OH)_3$	$Fe(II)_{aq}$	anaerobic photosynthesis	-1.5 ± 0.2		Croal et al. (2004)
dto.	dto.	abiotic	-1.0		Bullen et al. (2001)
Fe_2O_3, FeO(OH)	$Fe(II)_{aq}$	DIR, equilibrium	-3.0		Crosby et al. (2007)
$Fe(III)_{aq}$	Fe_2O_3	equilibrium[1]		+0.1 ± 0.2	Skulan et al. (2002)
$Fe(II)_{aq}$	Fe_3O_4	DIR, equilibrium	+1.3 ± 0.1		Johnson et al. (2005)
$Fe(II)_{aq}$	Fe_3O_4	magnetotactic bacteria	0		Mandernack et al. (1999)
$Fe(II)_{aq}$	$FeCO_3$	DIR, equilibrium	0		dto.
$Fe(II)_{aq}$	$FeCO_3$	abiotic	-0.5 ± 0.2		Wiesli et al. (2004)
$Fe(II)_{aq}$	$Ca_{0.15}Fe_{0.85}CO_3$	DIR, equilibrium	-0.9		Johnson et al. (2005)
Fe_3O_4	$FeCO_3$	DIR, equilibrium	-1.3		dto.
Fe_3O_4	$Ca_{0.15}Fe_{0.85}CO_3$	DIR, equilibrium	-2.2		dto.
Fe_3O_4	$FeCO_3$	equilibrium	-1.8		Johnson et al.(2008) based on Johnson et al. (2005) and Wiesli et al. (2004)
Theoretical approaches			**T= 22°C**	**T= 200°C**	
$Fe(II)_{aq}$	$Fe(III)_{aq}$	equilibrium[2]	+2.5 to +3.0	+1.1 to +1.2	Anbar (2005)
$Fe(II)_{aq}$	Fe_3O_4	equilibrium[2]	+0.3 to -0.8	+0.1 to -0.4	based on Polyakov et al. (2007), Mineev et al. (2007) and Anbar (2005)
$Fe(III)_{aq}$	Fe_3O_4	equilibrium[2]	-2.3 to -3.6	-1.0 to -1.6	dto.
Fe_2O_3	Fe_3O_4	equilibrium[2]	-0.9 to -1.8	-0.3 to -0.7	based on Polyakov and Mineev (2000), Polyakov et al. (2007) and Mineev et al. (2007)
Fe_3O_4	$FeCO_3$	equilibrium[2]	-1.8 to -2.8	-0.8 to -1.2	dto.
$Fe(II)_{aq}$	$FeCO_3$	equilibrium[2]	-2.5 to -2.6	-1.1	based on Polyakov and Mineev (2000) and Anbar (2005)
$Fe(II)_{aq}$	$CaFe_{0.5}Mg_{0.5}(CO_3)_2$	equilibrium[2]	-4.0 to -4.1	-1.7	dto.
$Fe(II)_{aq}$	$Ca_{1.1}Mg_{0.5}Fe_{0.3}Mn_{0.1}(CO_3)_2$	equilibrium[2]	-3.0 to -3.2	-1.3	dto.

(1) A kinetic fractionation factor that was lower by 1 to 2‰ was documented for this reaction in the same study.
(2) Range is defined by $Fe(III)_{aq}$ and $Fe(II)_{aq}$ estimates that are from both DFT-PCM and DFT, while magnetite estimates are from both Mössbauer and INRXS (see references).